Global organization of phase space in the transition to chaos in the Lorenz system

Eusebius J. Doedel
Department of Computer Science, Concordia University,
1455 Boulevard de Maisonneuve O., Montréal, Québec H3G 1M8, Canada

Bernd Krauskopf and Hinke M. Osinga
Department of Mathematics, The University of Auckland,
Private Bag 92019, Auckland 1142, New Zealand

December 2014

Abstract

The transition to chaos in the Lorenz system — from simple via preturbulent to chaotic dynamics — has been characterized in terms of the dynamics on the respective attractors, as described by the one-dimensional Lorenz map. In this paper we consider how this transition manifests itself globally, that is, we determine the associated organization of the entire phase space. To this end, we study how global invariant manifolds of equilibria and periodic orbits change with the parameters; the main object of study in this context is the two-dimensional stable manifold of the origin, or Lorenz manifold. Two-dimensional global manifolds and their complicated intersection sets with a plane or sphere are calculated with a boundary-value-problem setup. This allows us to determine how basins of attraction change or are created, and to give a precise characterization of the observed topological and geometric properties of the relevant invariant manifolds during the transition. In particular, we show where preturbulence occurs after the first homoclinic bifurcation and how it suddenly disappears in a heteroclinic bifurcation to give rise to a chaotic attractor and its basin.

1 Introduction

Edward N. Lorenz derived in the 1960s a much simplified model of convection dynamics in the atmosphere that bears his name today [33]. The Lorenz system is the vector field in $\mathbb{R}^3$ given by

$$\left\{ \begin{array}{rcl} \dot{x} & = & \sigma(y-x), \\ \dot{y} & = & \varrho x - y - xz, \\ \dot{z} & = & xy - \beta z, \end{array} \right. \tag{1}$$

where $\varrho, \sigma, \beta \in \mathbb{R}$ are parameters. System (1) is invariant under the transformation

$$(x, y, z) \mapsto (-x, -y, z),$$

which means that any solution is either symmetric under rotation by π about the z-axis (such as the Lorenz attractor), or has a corresponding symmetric counterpart. Famously, Lorenz found sensitive dependence on initial conditions — the property that is the hallmark of chaotic dynamics — for the now classic parameters values of $\sigma = 10$, $\beta = 8/3$, and $\varrho = 28$; the associated butterfly-shaped Lorenz attractor is probably the best known example of a chaotic attractor.

We are concerned with the transition from simple to chaotic dynamics as the parameter ϱ is changed in the range $(0, 30)$, while $\sigma = 10$ and $\beta = 8/3$ are kept fixed. Figure 1 is the corresponding one-parameter bifurcation diagram of (1) in the (ϱ, x)-plane, showing its equilibria $\mathbf{0}$, p^+ and p^- and the pair of bifurcating periodic orbits Γ^+ and Γ^-. The origin $\mathbf{0}$ is always an equilibrium; it is stable and the only attractor for $\varrho \in (0, 1)$, and

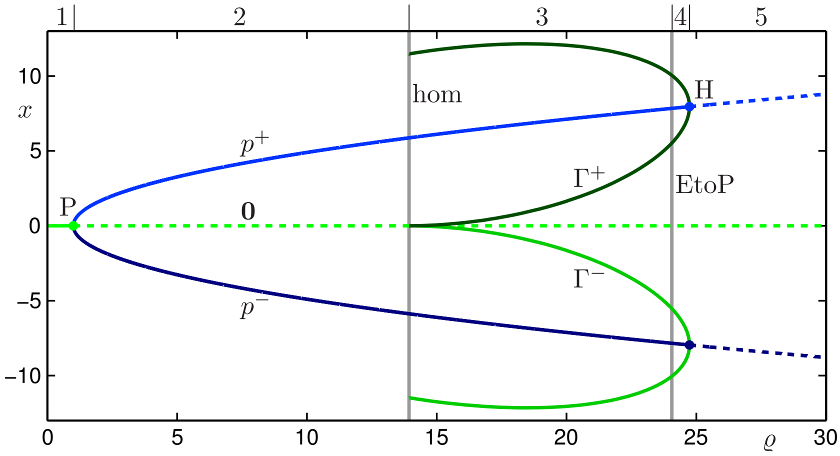

Figure 1: The bifurcation diagram of (1) in ϱ of the equilibria $\mathbf{0}$ and $p^{\pm}$ and the saddle periodic orbits $\Gamma^{\pm}$, featuring a pitchfork bifurcation of $\mathbf{0}$ at $\varrho_{\mathrm{P}} = 1$, a homoclinic bifurcation at $\varrho_{\mathrm{hom}} \approx 13.9265$, an EtoP heteroclinic connection at $\varrho_{\mathrm{het}} \approx 24.0579$, and a Hopf bifurcation of $p^{\pm}$ at $\varrho_{\mathrm{H}} = \frac{470}{19} \approx 24.7368$; the numbers at the top indicate the different regimes.

bifurcates at the pitchfork bifurcation P at $\varrho = \varrho_P = 1$. For $1 < \varrho$ the equilibrium $\mathbf{0}$ is a saddle with two real stable eigenvalues and one real unstable eigenvalue. Hence, it has a one-dimensional unstable manifold $W^u(\mathbf{0})$, consisting of all points in phase space that converge to $\mathbf{0}$ for $t \to -\infty$, and a two-dimensional stable manifold $W^s(\mathbf{0})$, consisting of all points that converge to $\mathbf{0}$ for $t \to \infty$. In light of its important role for the overall organization of phase space, we refer to $W^s(\mathbf{0})$ as the Lorenz manifold. At ϱ_P the two symmetrically related stable equilibria

$$p^{\pm} = \left(\pm\sqrt{\beta(\varrho - 1)}, \pm\sqrt{\beta(\varrho - 1)}, \varrho - 1\right)$$

emerge. The points $p^{\pm}$ lose their stability in the Hopf bifurcation H at

$$\varrho = \varrho_H = \frac{\sigma\,(\beta + \sigma + 3)}{\sigma - \beta - 1} = \frac{470}{19} \approx 24.7368,$$

where they become saddle foci. The Hopf bifurcation H is subcritical and gives rise to the symmetrically related pair of saddle periodic orbits $\Gamma^{\pm}$, which exist for $\varrho < \varrho_H$; in figure 1 they are represented by their maximum and minimum x-values. As ϱ is decreased from ϱ_H, the periodic orbits $\Gamma^{\pm}$ persist until they reach the origin $\mathbf{0}$ to form a pair of homoclinic orbits at

$$\varrho = \varrho_{\mathrm{hom}} \approx 13.9265.$$

At this parameter value, the unstable manifold $W^u(\mathbf{0})$ is contained in the Lorenz manifold $W^s(\mathbf{0})$. This point is also referred to as the homoclinic explosion point, because it creates a hyperbolic set or chaotic saddle $\mathcal{S}$ that contains, in particular, infinitely many other saddle periodic orbits [17, 20, 42]. Importantly, immediately past ϱ_{hom} the sinks $p^{\pm}$ remain the only attractors of (1). The chaotic attractor is created only at

$$\varrho = \varrho_{\mathrm{het}} \approx 24.0579,$$

where $W^u(\mathbf{0})$ forms a pair of heteroclinic connections from the equilibrium $\mathbf{0}$ to the periodic orbits $\Gamma^{\pm}$. At this bifurcation, which we refer to as an EtoP connection for short, the two branches of $W^u(\mathbf{0})$ lie in the two-dimensional stable manifolds $W^s(\Gamma^{\pm})$. Immediately past ϱ_{het}, the Lorenz system (1) exhibits multistability, because the chaotic attractor coexists with the two sinks $p^{\pm}$ for $\varrho_{\mathrm{het}} < \varrho < \varrho_H$, that is, until $p^{\pm}$ become saddles at the Hopf bifurcation H.

Overall, the four bifurcations P, hom, EtoP and H are responsible for the transition from simple to chaotic dynamics of (1), and they divide the ϱ-range $(0, 30)$ in figure 1 into five intervals, labelled 1–5. The knowledge of the attracting or long-term dynamics of the Lorenz system, especially in the preturbulent regime 4 and in the turbulent or chaotic regime 5, comes from the description of the dynamics on the attractor by a one-dimensional map, generally referred to as the Lorenz map. The construction of this map relies on geometric conditions that abstract what has been observed in the Lorenz system: the attractor intersects the Poincaré section $\Sigma_\rho = \{z = \rho - 1\}$, which contains $p^\pm$, in infinitely many lines, but these are extremely close together. A technical assumption of the abstract geometric Lorenz model is that there is a stable invariant foliation in the section, meaning that its leaves map to leaves and points are contracted along leaves towards the attractor. Then the one-dimensional Lorenz map describes how leaves map to leaves in the stable foliation and, hence, describes exactly the dynamics on the attractor — one speaks of the geometric Lorenz model. This construction/reduction was developed by Guckenheimer [19] in 1976 and subsequently by Guckenheimer and Williams [21] and Williams [45] in 1979, and also independently by Afrajmovich, Bykov and Shil'nikov [2] in 1977. Famously, Tucker [43] proved only in 1999 that the Lorenz system (1) actually satisfies the relevant geometric conditions for the classic parameter values $\sigma = 10$, $\beta = 8/3$, and $\varrho = 28$; see also [44].

The study of the Lorenz map made it possible to determine many properties of the Lorenz attractor. In 1979 Kaplan and Yorke [24] studied the dynamics of the Lorenz system past the homoclinic bifurcation, in what we call region 4 with $\varrho_{\mathrm{hom}} < \varrho < \varrho_{\mathrm{het}}$. They found that there are trajectories with arbitrarily long transients before they settle down to either p^+ or p^-, which are the only attractors. In analogy with the notion of turbulence introduced by Ruelle and Takens [39], Kaplan and Yorke called this type of dynamics preturbulence, which they showed is due to the existence of a Smale horseshoe in the Poincaré map. The statistical properties of preturbulence were subsequently investigated in a numerical study of the Lorenz map [46].

The purpose of this paper is to clarify how this transition manifests itself throughout phase space. In other words, we wish to answer the following questions. How is the dynamics on the attractor, whether it is simple, preturbulent or chaotic, expressed in terms of the overall organization of the Lorenz system? What are the basins of attraction and their boundaries in $\mathbb{R}^3$? And more specifically, where can preturbulence be found in phase space, and where does the basin of attraction of the chaotic attractor come from?

The key to the overall organization of phase space is the study of two-dimensional global invariant manifolds, because these surfaces form separatrices in the three-dimensional phase space of the Lorenz system. Of special importance is the Lorenz manifold $W^s(\mathbf{0})$. In region 2 the surface $W^s(\mathbf{0})$ forms the entire boundary between the two basins of p^+ and p^-. However, in spite of the fact that p^+ and p^- remain the only two attractors, past the homoclinic bifurcation at ϱ_{hom}, in region 3 of preturbulence, this is no longer the case. Rather, the boundary of the basins of p^+ and p^- is also formed by the stable manifold of the chaotic saddle, which can be found as the closure of the two-dimensional stable manifolds $W^s(\Gamma^\pm)$ of the two bifurcating periodic orbits $\Gamma^\pm$; this was shown in [15] and is reviewed in section 2. We then proceed by studying how these sets change and occupy an increasingly larger part of phase space on the way to the heteroclinic EtoP bifurcation. We then show how the chaotic attractor and its basin are created in the EtoP bifurcation, which we identify as a boundary crisis bifurcation. Moreover, we show how $W^s(\mathbf{0})$ lies dense in the basin of the chaotic attractor. In our investigation of the global properties of this transition to chaos in the Lorenz system, we characterize the properties of the two-dimensional manifolds $W^s(\mathbf{0})$ and $W^s(\Gamma^\pm)$ by considering their intersection sets with a sufficiently large sphere. In particular, we show that in the region of preturbulence the intersection set of $W^s(\Gamma^\pm)$ is the accessible boundary of an indecomposible continuum, which grows to become the basin of the chaotic attractor.

The results presented here are made possible by the develoment of dedicated numerical techniques for the computation of two-dimensional global invariant manifolds and their intersection sets, and a secondary goal of this paper is to showcase such state of the art computations. From the very beginning, numerical calculations have played a crucial role for furthering the understanding of the Lorenz system. Indeed, Lorenz himself discovered the sensitive dependence on the initial condition of (1) in his computer simulations quite by accident [16]. Moreover, his numerical explorations allowed him to make a topological sketch of the Lorenz attractor [33]. The development of the geometric Lorenz attractor and the 1D Lorenz map was also based on and checked with careful numerical simulations [2, 19, 21]. Tucker's proof employed interval arithmetic calculations to obtain relevant estimates [43].

The two-dimensional Lorenz manifold $W^s(\mathbf{0})$ has received attention because of its role in organizing the dynamics of (1). Already in 1979 Perelló [37] considered how $W^s(\mathbf{0})$ changes through the homoclinic bifurcation at ϱ_{hom} and provided sketches (reproduced in [14]) of $W^s(\mathbf{0})$ at and after this bifurcation; this work was based on numerical simulations by Simó [41]. Perelló's sketch past the homoclinic bifurcation formed the basis of the illustrations by Abraham and Shaw [1] of $W^s(\mathbf{0})$ for $\varrho = 28$ (reproduced in [35]). In 1985 Jackson studied the basins of p^+ and p^-, and provided hand-drawn sketches of $W^s(\mathbf{0})$ near the origin, both for $\varrho < \varrho_{\rm hom}$ [22] and for $\varrho_{\rm hom} < \varrho$ [23]. All these early renderings of the Lorenz manifold are based on extensive and careful numerical simulations; effectively, $W^s(\mathbf{0})$ was obtained indirectly as the complement of points that converge to either p^+ or p^-.

More recently, numerical methods have been developed that allow one to compute a two-dimensional global invariant manifold directly. The Lorenz system has been a testbed for these developments, with the challenge being to compute the Lorenz manifold $W^s(\mathbf{0})$. Today there are several implemented methods; most of them are presented in the survey [31], where the Lorenz manifold is used to discuss and compare the properties of the different approaches. The underlying idea is to start from local information near a saddle equilibrium or periodic orbit and then to globalize or grow the manifold. The computations presented in this paper make use of the general technique of finding a family of orbit segments defined by a suitably posed two-point boundary value problem (2PBVP); see [31] for background information. The two-dimensional manifold $W^s(\mathbf{0})$ is computed as a surface formed by a family of geodesic level sets; this approach is described in detail in [28, 29]. Additionally, we compute large sets of intersection curves of the stable manifolds $W^s(\mathbf{0})$ and $W^s(\Gamma^\pm)$ with a sufficiently large sphere via a suitable 2PBVP setup; see section 5 for details.

We make extensive use of these techniques to gain insight into the topological and geometric structure of global invariant manifolds in the Lorenz system, and how these change with the parameter ϱ. This allows us to make precise observations regarding the overall organization of phase space during the transition to chaos. Strictly speaking, these observations are conjectures that are supported by detailed numerical evidence. In the spirit of previous work on the Lorenz system, we hope that the results presented here will inspire further investigations.

The paper is organized as follows. In section 2 we review the transition through the homoclinic bifurcation into preturbulence. Section 3 discusses how the structure associated with preturbulence grows, and section 4 presents the transition through the EtoP bifurcation and the creation of the chaotic attractor. In Section 5 we introduce and discuss the boundary value problem setup for the calculation of many intersection curves of manifolds, including their isolas. The final section 6 contains an overall mathematical characterization of the transition to chaos, as well as a brief outlook.

2 Into the preturbulent regime

The transition to chaos starts with a homoclinic bifurcation at $\varrho_{\rm hom} \approx 13.9265$, which gives rise to the so-called preturbulent regime. The homoclinic bifurcation is illustrated in figure 2 in terms of the one-dimensional unstable manifold $W^u(\mathbf{0})$ of the origin $\mathbf{0}$; also shown are the one-dimensional strong stable manifolds $W^{ss}(p^+)$ and $W^{ss}(p^-)$ of the sinks $p^\pm$, which are defined by the direction of strongest contraction. The disk represents the linear stable eigenspace $E^s(\mathbf{0})$ spanned by the two stable eigenvalues of $\mathbf{0}$. Figure 2 (a) shows the situation before the homoclinic bifurcation, where the right-hand branch of the unstable manifold $W^u(\mathbf{0})$ of the origin $\mathbf{0}$ spirals into p^+ and the left-hand branch of $W^u(\mathbf{0})$ spirals into p^-. At the moment of bifurcation, shown in figure 2(b), both branches of $W^u(\mathbf{0})$ connect back to $\mathbf{0}$ tangent to $E^s(\mathbf{0})$ and form a symmetrically related pair of homoclinic connecting orbits. Panel (c) shows the situation after the homoclinic bifurcation, where the right-hand branch of $W^u(\mathbf{0})$ now spirals into p^- and the left-hand branch of $W^u(\mathbf{0})$ spirals into p^+. Moreover, two saddle periodic orbits, Γ^+ and Γ^-, have been created from the two homoclinic connections. Note that the manifolds $W^{ss}(p^\pm)$ do not change qualitatively in this homoclinic bifurcation.

While Figure 2 clearly shows that there is a homoclinic bifurcation and that it creates two periodic orbits, it does not really explain its consequences for the dynamics of the Lorenz system after the bifurcation. In fact, the two points p^+ and p^- remain the only attractors of (1) and the complicated dynamics created at $\varrho_{\rm hom} \approx 13.9265$ is initially of saddle type [21]. It was realized in [24] from the study of the one-dimensional Lorenz map that, as a consequence, for $\varrho_{\rm hom} < \varrho < \varrho_{\rm het}$ one may find trajectories with arbitrarily long chaotic transients before either p^+ or p^- are finally reached; one speaks of the preturbulent regime.

In order to understand the geometric organization of phase space that explains preturbulent dynamics it is necessary to consider the associated two-dimensional stable manifolds $W^s(\mathbf{0})$ and $W^s(\Gamma^\pm)$. As we will see in section 4, the manifolds $W^s(\mathbf{0})$ and $W^s(\Gamma^\pm)$ also play an important role in the subsequent creation of the chaotic attractor and its basin at the EtoP connection, when $\varrho_{\rm het} \approx 24.0579$. We first review here how these surfaces change through the homoclinic bifurcation at $\varrho_{\rm hom} \approx 13.9265$; see also [15].

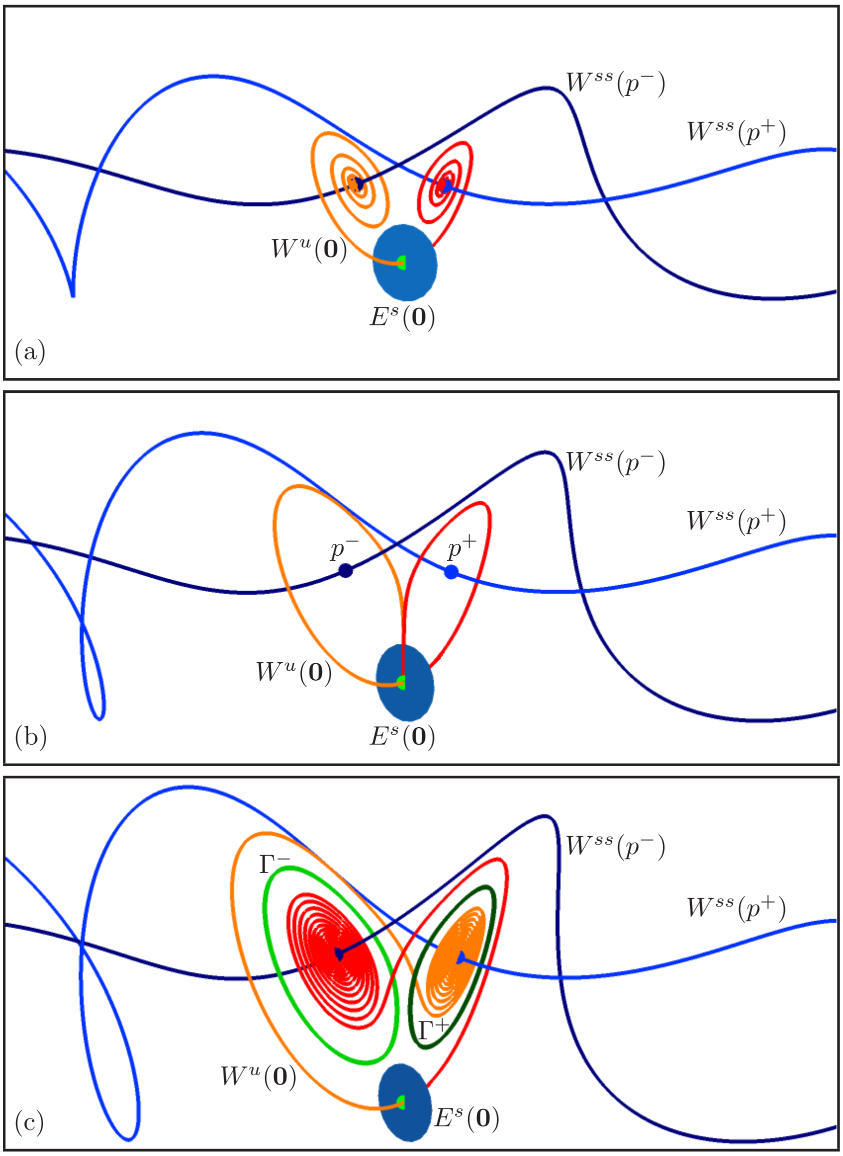

Figure 2: The transition through the homoclinic bifurcation at $\varrho_{\text{hom}} \approx 13.9265$. Shown are $\mathbf{0}$, $p^\pm$, $\Gamma^\pm$, $W^u(\mathbf{0})$, $W^{ss}(p^\pm)$, and a small disk in the linear eigenspace $E^s(\mathbf{0})$, for $\varrho = 10.0$ (a), for $\varrho = 13.9265$ (b), and for $\varrho = 18.0$ (c).

Figure 3 shows the global invariant manifolds for $\varrho = 10.0$, which is representative for the situation before the homoclinic bifurcation, that is, for $1 < \varrho < \varrho_{\text{hom}}$. Panel (a) shows the first part of the Lorenz manifold $W^s(\mathbf{0})$, computed up to geodesic distance 262.0, that lies in the region of negative y. The surface $W^s(\mathbf{0})$ divides the phase space into the two basins of attraction, $\mathcal{B}(p^+)$ of p^+ and $\mathcal{B}(p^-)$ of p^-, meaning that the trajectory of any initial condition not on $W^s(\mathbf{0})$ will end up at either p^+ or p^-. The points $p^\pm$ and the one-dimensional manifolds $W^u(\mathbf{0})$ and $W^{ss}(p^\pm)$ are shown in the centre; compare with figure 2(a). Notice in figure 3(a) how the surface $W^s(\mathbf{0})$ spirals around the curves $W^{ss}(p^\pm)$. In [15], we found that it suffices to consider the intersection set $\widehat{W}^s(\mathbf{0}) := W^u(\mathbf{0}) \cap S_R$ with a sphere S_R in order to understand the overall organization of phase space. This sphere S_R must be large enough so that it intersects only the unbounded global invariant manifolds; in particular, $W^u(\mathbf{0})$ should be contained in its interior. As in [15] and as shown in figure 3(a), we choose $(0, 0, \varrho-1)$ as the centre of S_R and its radius R is such that the second intersection point of the low-amplitude branch of $W^{ss}(p^\pm)$ with the plane Σ_ϱ lies on the equator of S_R. Figure 3(b) shows how the sphere S_R is divided by $\widehat{W}^s(\mathbf{0})$

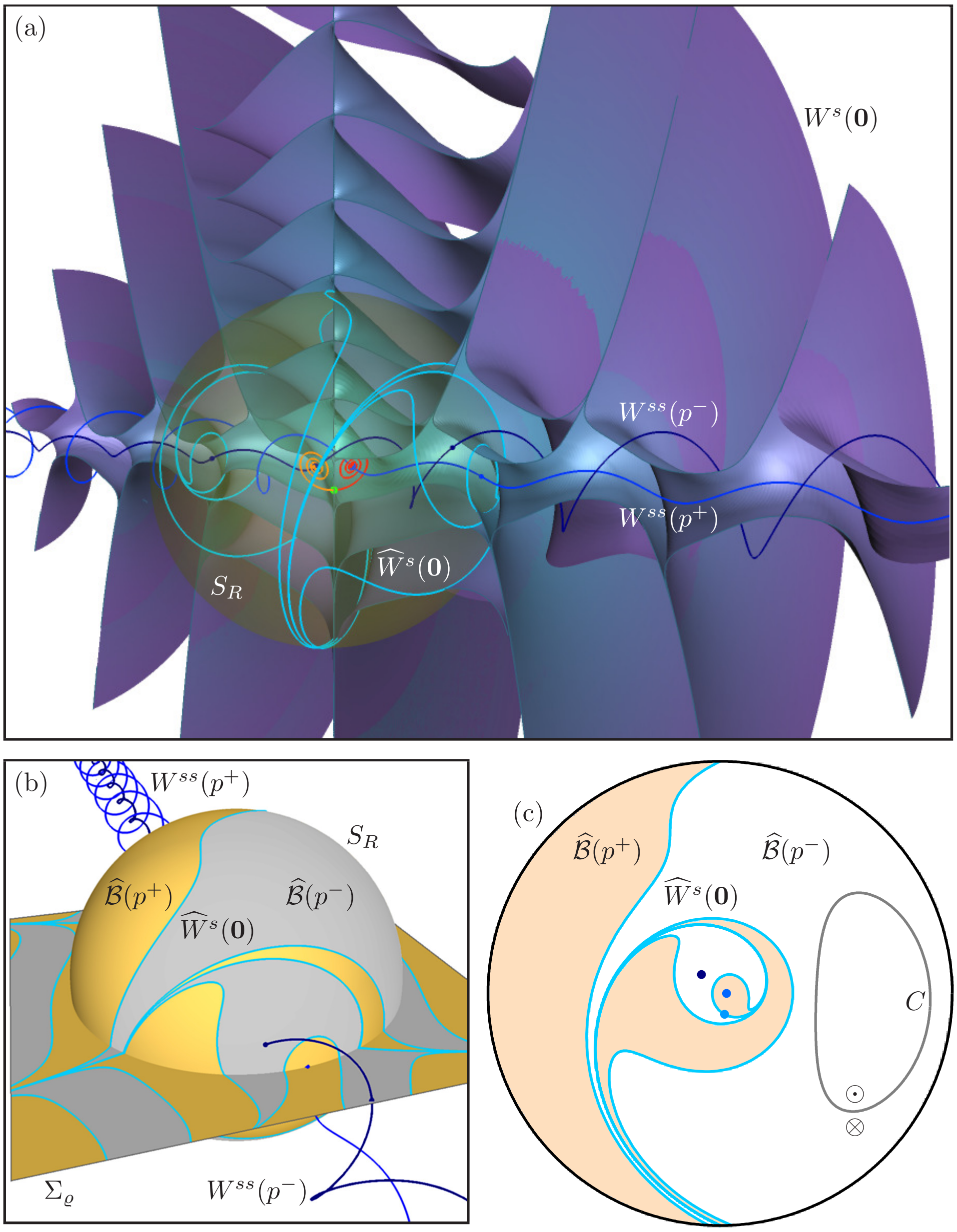

Figure 3: The organization of phase space for $\varrho = 10.0$. Panel (a) shows the part of $W^s(\mathbf{0})$, computed up to geodesic distance 262.0, that lies in the region of negative y, together with $\mathbf{0}$, $p^{\pm}$, $W^u(\mathbf{0})$, $W^{ss}(p^{\pm})$, the sphere S_R with $R = 67.156$ and the intersection set $\widehat{W}^s(\mathbf{0})$ (light blue) on it. Panel (b) shows how $\widehat{W}^s(\mathbf{0})$ divides S_R into the basins $\widehat{\mathcal{B}}(p^+)$ (sand colour) and $\widehat{\mathcal{B}}(p^-)$ (white), and how these sets connect up with the corresponding basins on the plane Σ_ϱ. Panel (c) is the stereographic projection of S_R for $x \geq 0$; also shown are $\widehat{W}^{ss}(0)$ (light blue dot), $\widehat{W}^{ss}(p^+)$ (blue dot) and $\widehat{W}^{ss}(p^-)$ (dark blue dot) and the tangency locus C with the symbols $\otimes$ and $\odot$ indicating the direction of the vector field. See also the accompanying animation dko_tochaos_a01.gif available via the Supplementary Data link.

into two disjoint basins $\widehat{\mathcal{B}}(p^+) := \mathcal{B}(p^+) \cap S_R$ and $\widehat{\mathcal{B}}(p^-) := \mathcal{B}(p^+) \cap S_R$; also shown are the corresponding intersection sets on the plane Σ_ϱ. We can now deduce the main properties of $W^s(\mathbf{0})$ from how it intersects S_R. Because of the rotational symmetry of the Lorenz system, it suffices to consider only one half of S_R. We chose the half with $x \geq 0$, which can be represented in a convenient way by means of the stereographic projection

$$(u, v) := \left(\frac{y}{x+R}, \frac{z-(\varrho-1)}{x+R} \right), \tag{2}$$

where $x^2 + y^2 + (z - \varrho + 1)^2 = R^2$. Figure 3(c) shows this stereographic projection of S_R to illustrate how $\widehat{W}^s(\mathbf{0})$ divides it into $\widehat{\mathcal{B}}(p^+)$ and $\widehat{\mathcal{B}}(p^-)$. Here we also plot the tangency locus C, which divides S_R into regions where the vector field points inwards (denoted by $\otimes$) and outwards (denoted by $\odot$), respectively; note that C lies entirely inside $\widehat{\mathcal{B}}(p^-)$ for $\varrho = 10$.

The main conclusion from figure 3 is that, for $1 < \varrho < \varrho_{\rm hom}$, the intersection set $\widehat{W}^s(\mathbf{0})$ is a single closed curve! This may not be obvious, but can be checked by close inspection of figure 3(c). Our computation of $\widehat{W}^s(\mathbf{0})$ confirms that the associated family of orbits segments provides a smooth one-to-one mapping from a small ellipse in $E^s(\mathbf{0})$ around $\mathbf{0}$ to $\widehat{W}^s(\mathbf{0})$; we refer to section 5 and [15]. It follows that $\widehat{\mathcal{B}}(p^+)$ and $\widehat{\mathcal{B}}(p^-)$ are two topological disks.

Figure 4 illustrates the situation after the homoclinic bifurcation, that is, for $\varrho_{\rm hom} < \varrho < \varrho_{\rm het}$, for the specific case of $\varrho = 18.0$. Panel (a) shows the first part of $W^s(\mathbf{0})$, computed up to geodesic distance 150.5, that lies in the region of negative y. As before, we also plot the points $p^\pm$ and the one-dimensional manifolds $W^u(\mathbf{0})$ and $W^{ss}(p^\pm)$; compare with figure 2(c). The surface $W^s(\mathbf{0})$ intersects S_R again in the intersection set $\widehat{W}^s(\mathbf{0})$, but this set is no longer a single closed curve. Rather, $\widehat{W}^s(\mathbf{0})$ consists of infinitely many curves that appear to cover some 'bands' on S_R. These bands are further illustrated in figure 4(b), where we show the computed manifold $W^s(\mathbf{0})$ only up to its intersection with S_R and similarly cropped the one-dimensional manifolds $W^{ss}(p^\pm)$ up to their respective intersection points with S_R. Our computations of $\widehat{W}^s(\mathbf{0})$ confirm these results; see section 5 for more details. Figure 4(c) shows the intersection sets $\widehat{W}^s(\mathbf{0})$, $\widehat{W}^s(\Gamma^+) := W^s(\Gamma^+) \cap S_R$ and $\widehat{W}^s(\Gamma^-) := W^s(\Gamma^-) \cap S_R$ on the stereographic projection of S_R for $x \geq 0$. Even though we can only plot a finite number of curves, each of these three intersection sets consist of infinitely many curves.

It is important to realize that $W^s(\mathbf{0})$ alone no longer divides the phase space into the two basins $\mathcal{B}(p^+)$ and $\mathcal{B}(p^-)$ [3, 15]. Namely, close to p^+ the boundary of $\mathcal{B}(p^+)$ is formed by the stable manifold $W^s(\Gamma^+)$, which is locally a cylinder; similarly, $W^s(\Gamma^-)$ forms a boundary of $\mathcal{B}(p^-)$ near p^-. In particular, note the closed curve in $\widehat{W}^s(\Gamma^+)$ that surrounds the point in $\widehat{W}^{ss}(p^+)$ in the centre of figure 4(c); the equivalent situation occurs for $\widehat{W}^s(\Gamma^-)$ and $\widehat{W}^{ss}(p^-)$ on the other side of S_R, where $x \leq 0$. All other, infinitely many more curves in $\widehat{W}^s(\Gamma^+)$ and $\widehat{W}^s(\Gamma^-)$ are arcs whose ends accumulate on either of these two closed curves. We call the (sand-coloured) disk in figure 4(c) that is bounded by the closed curve in $\widehat{W}^s(\Gamma^+)$ the *primary* basin of p^+. There is another topological disk in $\widehat{\mathcal{B}}(p^+)$ that is part of the primary basin of p^+, namely, the region that contains the other point of $\widehat{W}^{ss}(p^+)$, which lies on the other side of S_R; we can see part of this topological disk in figure 4(c) as the two larger (sand-coloured) regions that 'spilled over' from the other side of S_R; the region on the left is bounded by one arc in $\widehat{W}^s(\Gamma^+)$ and a segment of the unit circle; this region continues onto the other side of S_R and is connected to the other comma-shaped (sand-coloured) region in figure 4(c), which is bounded by this same arc in $\widehat{W}^s(\Gamma^+)$ as well as by one arc in $\widehat{W}^s(\mathbf{0})$. These two arcs are special because points on them will go straight to Γ^+ or $\mathbf{0}$, respectively; that is, they are the intersections with S_R of the local stable manifolds of Γ^+ and $\mathbf{0}$, respectively; see also figure 4(b), which illustrates this for the local stable manifold of $\mathbf{0}$. Similarly, the primary basin of p^- is formed by the (white) disk bounded by the closed curve in $\widehat{W}^s(\Gamma^-)$ and the topological disk bounded by the symmetrically related arc in $\widehat{W}^s(\Gamma^-)$ and the same arc in $\widehat{W}^s(\mathbf{0})$ (which is itself symmetric); we can see part of the topological disk in the primary basin of p^- as the two relatively large white regions in figure 4(c), the smaller of which contains the point in $\widehat{W}^{ss}(p^-)$ just above the centre of the figure.

The complement of the primary basins of $p^\pm$ is the 'band' on S_R that contains the infinitely many other arcs of $\widehat{W}^s(\mathbf{0})$ and $\widehat{W}^s(\Gamma^\pm)$. This band comprises a finer structure of 'bands' and the curves in the set $\widehat{W}^s(\Gamma^+) \cup \widehat{W}^s(\Gamma^-)$ locally appear to form a Cantor set of curves. In fact, the intersection points of a line segment with $\widehat{W}^s(\Gamma^+) \cup \widehat{W}^s(\Gamma^-)$ bound intervals on this line segment in the complement of a Cantor set. Moreover, each such interval is divided by a point in $\widehat{W}^s(\mathbf{0})$ into two subintervals — one of which lies in $\widehat{\mathcal{B}}(p^+)$ and the other in $\widehat{\mathcal{B}}(p^-)$. Note that each and every intersection curve in $\widehat{W}^s(\mathbf{0})$ and $\widehat{W}^s(\Gamma^\pm)$ lies in the boundary of $\widehat{\mathcal{B}}(p^\pm)$, but only $\widehat{W}^s(\mathbf{0})$ and $\widehat{W}^s(\Gamma^+)$ ($\widehat{W}^s(\Gamma^-)$) are accessible from $\widehat{\mathcal{B}}(p^+)$ ($\widehat{\mathcal{B}}(p^-)$).

The overall conclusion is that the set $\widehat{W}^s(\Gamma^+) \cup \widehat{W}^s(\Gamma^-)$ is the accessible boundary of what is known as an

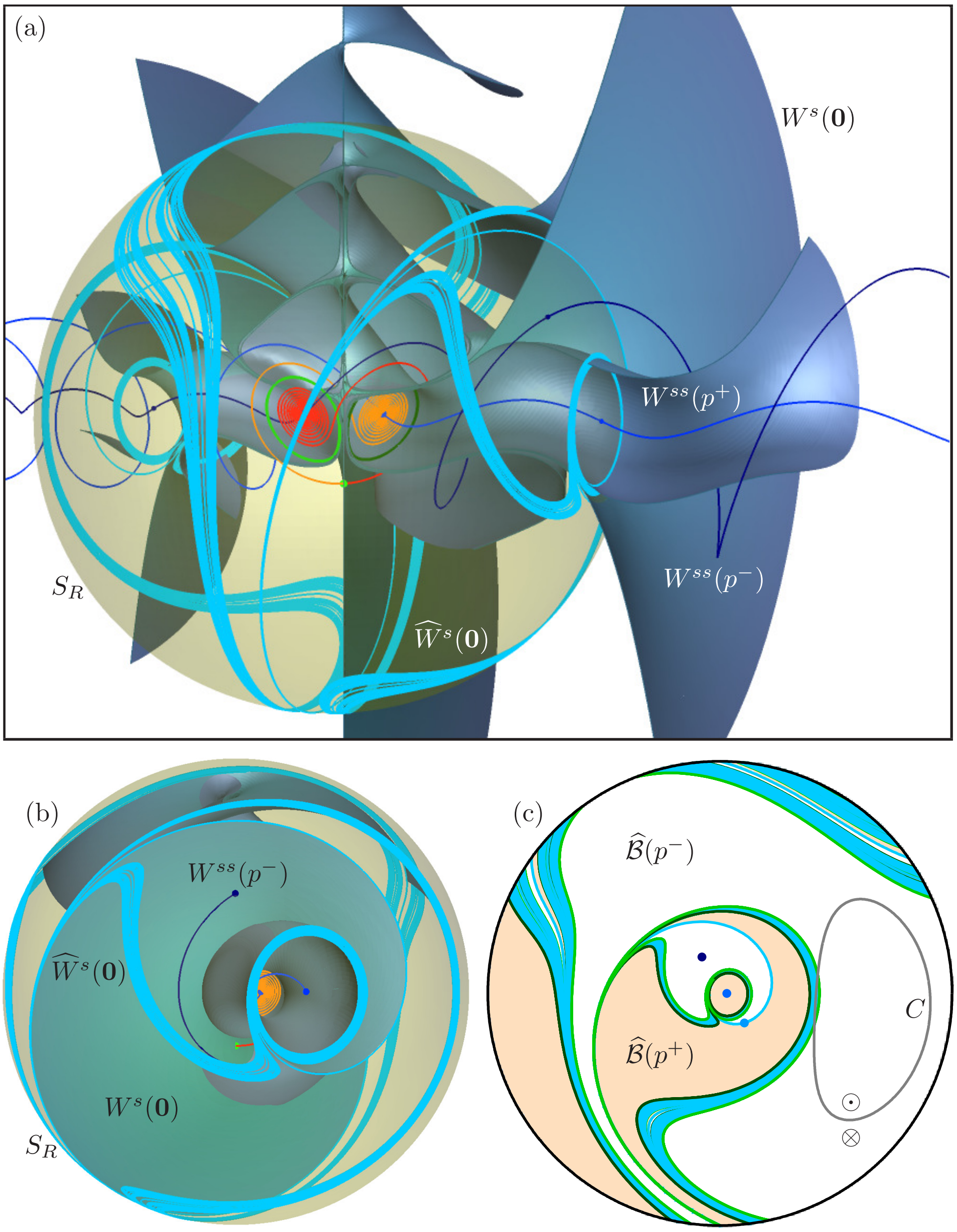

Figure 4: The organization of phase space for $\varrho = 18.0$. Panel (a) shows the part of $W^s(\mathbf{0})$, computed up to geodesic distance 150.5, that lies in the region of negative y, together with $\mathbf{0}$, $p^{\pm}$, $W^u(\mathbf{0})$, $W^{ss}(p^{\pm})$, the sphere S_R with $R = 69.062$ and the intersection set $\widehat{W}^s(\mathbf{0})$ (light blue) on it. Panel (b) shows $\widehat{W}^s(\mathbf{0})$ on S_R, together with the part of $W^s(\mathbf{0})$ that lies inside S_R. Panel (c) is the stereographic projection of S_R for $x \geq 0$, showing how the sets $\widehat{W}^s(\mathbf{0})$ (light blue), $\widehat{W}^s(\Gamma^+)$ (dark green) and $\widehat{W}^s(\Gamma^-)$ (light green) divide S_R into the basins $\widehat{\mathcal{B}}(p^+)$ (sand colour) and $\widehat{\mathcal{B}}(p^-)$ (white); also shown are $\widehat{W}^{ss}(0)$ (light blue dot), $\widehat{W}^{ss}(p^+)$ (blue dot) and $\widehat{W}^{ss}(p^-)$ (dark blue dot) and the tangency locus C with the symbols $\otimes$ and $\odot$ indicating the direction of the vector field. See also the accompanying animation dko_tochaos_a02.gif available via the Supplementary Data link.

indecomposable continuum [25, 26, 27, 40], that is, a nonempty connected compact metric space or continuum without proper subcontinua. This indecomposable continuum is the intersection set $\widehat{W}^s(\mathcal{S}) := W^s(\mathcal{S}) \cap S_R$ of the stable manifold of the saddle hyperbolic set $\mathcal{S}$ that is created in the homoclinic bifurcation. Since the two manifolds $W^s(\Gamma^{\pm})$ lie dense in $\mathcal{S}$ and each bounds one of the basins $\mathcal{B}(p^{\pm})$, we have that $\widehat{W}^s(\mathcal{S})$ is the closure

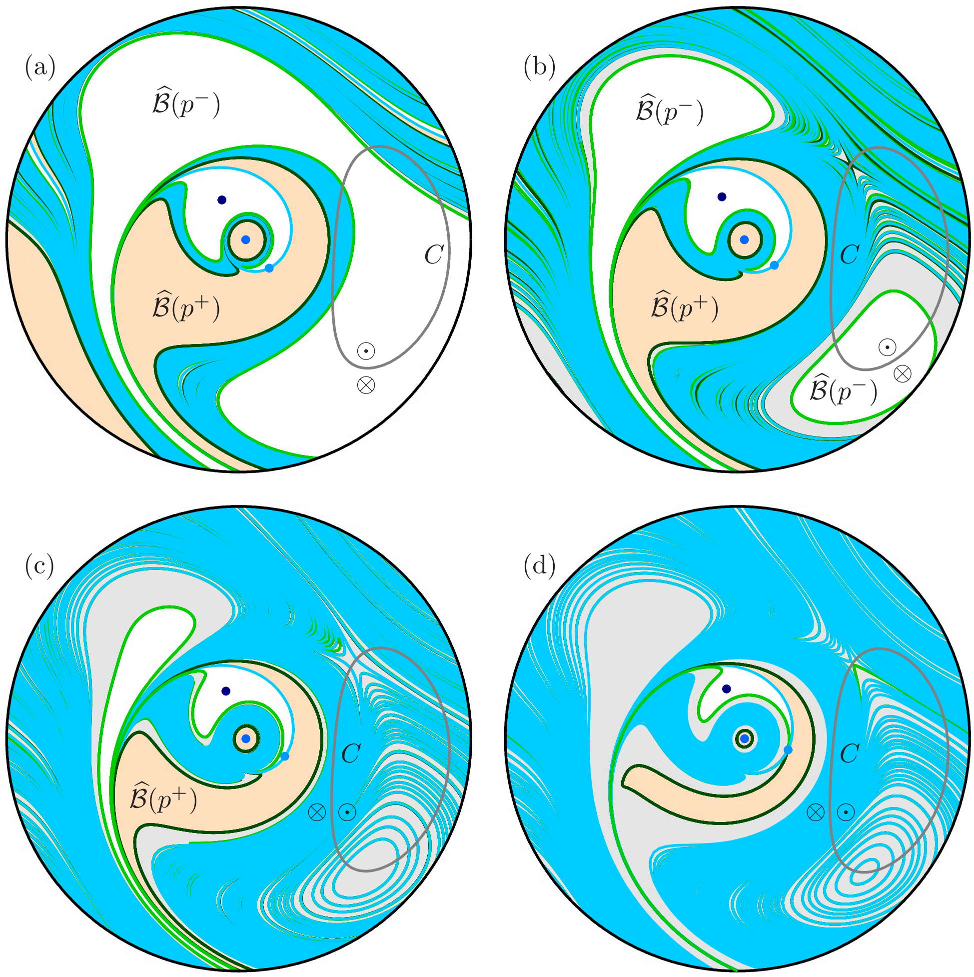

Figure 5: Stereographic projection of S_R for $x \geq 0$, for $\varrho = 19.5$ with $R = 69.346$ (a), for $\varrho = 21.0$ with $R = 69.612$ (b), for $\varrho = 23.0$ with $R = 69.947$ (c), and for $\varrho = 24.047$ with $R = 70.116$ (d), showing how the sets $\widehat{W}^s(\mathbf{0})$ (light blue), $\widehat{W}^s(\Gamma^+)$ (dark green) and $\widehat{W}^s(\Gamma^-)$ (light green) divide S_R into the basins $\widehat{\mathcal{B}}(p^+)$ (sand colour) and $\widehat{\mathcal{B}}(p^-)$ (white); the region of preturbulence is shaded grey. Also shown are $\widehat{W}^{ss}(0)$ (light blue dot), $\widehat{W}^{ss}(p^+)$ (blue dot) and $\widehat{W}^{ss}(p^-)$ (dark blue dot) and the tangency locus C with the symbols $\otimes$ and $\odot$ indicating the direction of the vector field.

of $\widehat{W}^s(\Gamma^+) \cup \widehat{W}^s(\Gamma^-)$.

3 Growing preturbulence

We reported in [15] that the indecomposable continuum $\widehat{W}^s(\mathcal{S})$ is created at the homoclinic bifurcation. Here we present how it changes with ϱ and then bifurcates at the EtoP bifurcation. Initially, when it is created at ϱ_{hom}, the indecomposable continuum $\widehat{W}^s(\mathcal{S})$ is initially small on the sphere S_R; specifically, its Hausdorff dimension goes to zero as $\varrho \searrow \varrho_{\text{hom}}$. However, as ϱ is increased towards ϱ_{het}, the indecomposable continuum $\widehat{W}^s(\mathcal{S})$ spreads over a larger area of S_R. This is illustrated in figure 5. Figure 5(a) shows a case similar to figure 4(c), but now ϱ has increased to 19.5, so that the area of the complement of the primary basins of $p^{\pm}$ has grown. As a result, (infinitely) many more curves of these intersection sets intersect the tangency locus C in figure 5(a). As ϱ is increased further, the single arc of $\widehat{W}^s(\Gamma^+)$ in the primary basin of p^- splits into two parts at $\varrho \approx 19.8530$ in a first saddle transition S at a single point on the tangency locus C. (The same happens to the symmetrically related arc of $\widehat{W}^s(\Gamma^+)$ on the other side of S_R.) Since this boundary curve of $\widehat{\mathcal{B}}(p^-)$ is accumulated by curves of the indecomposable continuum, this first saddle transition is followed by infinitely many saddle transitions of other curves in $\widehat{W}^s(\mathbf{0})$, $\widehat{W}^s(\Gamma^+)$ and $\widehat{W}^s(\Gamma^-)$. Figure 5(b) shows an approximate saddle transition of an arc in $\widehat{W}^s(\Gamma^+)$ for $\varrho = 21.0$. The saddle transitions give rise to closed curves or isolas of these intersection sets, which surround a now separated large topological disk in the primary basin of p^-. This disjoint disk in the primary basin of p^- disappears at $\varrho \approx 21.4200$ in a first minimax transition M on the tangency locus C, followed by infinitely many minimax transitions of other curves in $\widehat{W}^s(\mathbf{0})$, $\widehat{W}^s(\Gamma^+)$ and $\widehat{W}^s(\Gamma^-)$. (Again, the same happens to $\widehat{W}^s(\Gamma^+)$ on the other side of S_R.) As a result, in figure 5(c) for $\varrho = 23.0$, the primary basins of $p^{\pm}$ again consist of two parts each, and the area with curves of the indecomposable continuum (shaded grey) has increased considerably on the sphere S_R. Figure 5(d) shows the situation for $\varrho = 24.047$ very close to the EtoP connection and illustrates that this area grows even further as ϱ is increased; specifically, the visible part of the (white) topological disk in the primary basin of p^- has been reduced to a single component on this side of S_R in panel (d).

The panels of figure 5 show hundreds of curves of the sets $\widehat{W}^s(\mathbf{0})$, $\widehat{W}^s(\Gamma^+)$ and $\widehat{W}^s(\Gamma^-)$, which were computed with the 2PBVP setup detailed in section 5. Note that the curves of $\widehat{W}^s(\Gamma^+)$ and $\widehat{W}^s(\Gamma^-)$ that bound the primary basins of p^+ and p^- can be computed readily for any value of ϱ, because these are the intersections of the respective local manifolds with S_R. It is much more challenging to find the other additional intersection curves. We use an approach that selects curves up to a prescribed maximum integration time. While our numerical method highlights the fractal nature of the structure of the intersection set, it is unable to fill all of the grey shaded area of preturbulence, which should be densely filled with curves. In particular, the accumulation of curves onto the arc $\widehat{W}^s(\Gamma^{\pm})$ in the primary basins requires rapidly increasing integration times that are not feasible numerically.

The emergence of isolas, that is, closed curves of $\widehat{W}^s(\mathbf{0})$, $\widehat{W}^s(\Gamma^+)$ and $\widehat{W}^s(\Gamma^-)$ in figure 5 is inevitable due to the presence of the tangency locus C on S_R. Isolas appear in saddle transitions and disappear again in minimax transtions, which are generic interactions of these curves with the tangency locus C [32]. It is important to realize that these interactions are due to the way S_R intersects the two-dimensional manifolds $W^s(\mathbf{0})$, $W^s(\Gamma^+)$ and $W^s(\Gamma^-)$, respectively. In particular, they do not constitute bifurcations of the two-dimensional manifolds themselves. Since the interactions of the many curves with the tangency locus C on S_R cannot be avoided, we present a convenient way to compute them in section 5.

4 Into the turbulent regime

The indecomposable continuum $\widehat{W}^s(\mathcal{S})$ associated with the saddle hyperbolic set $\mathcal{S}$ exists only in the preturbulent regime, which is the parameter interval $\varrho_{\text{hom}} < \varrho < \varrho_{\text{het}}$. That is, as ϱ increases through $\varrho_{\text{het}} \approx 24.0579$, the set $\widehat{W}^s(\mathcal{S})$ along with its accessible boundary $\widehat{W}^s(\Gamma^+) \cup \widehat{W}^s(\Gamma^-)$ undergoes a dramatic change and disappears as an indecomposale continuum. At this ϱ-value, two symmetric heteroclinic bifurcations occur, where there exists a pair of connecting orbits from $\mathbf{0}$ to $\Gamma^{\pm}$ (EtoP). The EtoP heteroclinic connection at ϱ_{het} generates a chaotic attractor as is illustrated in figure 6 in terms of the relative positions of the periodic orbits $\Gamma^{\pm}$ and the one-dimensional unstable manifold $W^u(\mathbf{0})$; also shown are the sinks $p^{\pm}$ and their one-dimensional strong stable manifolds $W^{ss}(p^{\pm})$. Panel (a) for $\varrho = 23.5$ shows the situation before the EtoP connection, which is topologically as figure 2(c); in particular, the right-hand branch of $W^u(\mathbf{0})$ spirals into the attracting point p^- and the left-hand branch of $W^u(\mathbf{0})$ spirals into the attracting point p^+. Notice that figure 6(a) is already near the EtoP connection, so that the left- and right-hand branches of $W^u(\mathbf{0})$ come quite close to the periodic orbits Γ^+ and Γ^-, respectively. At the moment of bifurcation, shown in figure 6(b), each branch of $W^u(\mathbf{0})$ actually connects to the respective saddle periodic orbit. Panel (c), after the EtoP heteroclinic bifurcation, shows that the two branches of $W^u(\mathbf{0})$ do not reach the attracting points p^+ and p^- any longer. As a result, $W^u(\mathbf{0})$ now accumulates on a newly created chaotic attractor. As for the homoclinic explosion, the manifolds $W^{ss}(p^{\pm})$ do not change qualitatively in this heteroclinic bifurcation.

Recall that the two-dimensional stable manifolds $W^s(\Gamma^{\pm})$ (which are not shown in figure 2) are cylinders close to the periodic orbits $\Gamma^{\pm}$. Hence, locally near $\Gamma^{\pm}$, the EtoP connection is characterized by the fact that the one-dimensional manifold $W^u(\mathbf{0})$ moves from the 'insides' of these cylinders, where the two sides of $W^u(\mathbf{0})$ accumulate on the attracting points p^+ and p^-, to their 'outsides' which prevent $W^u(\mathbf{0})$ from reaching p^+ and p^-. As figure 7 shows, this has a dramatic effect on the overall global manifolds $W^s(\Gamma^{\pm})$. Panels (a) and (b)

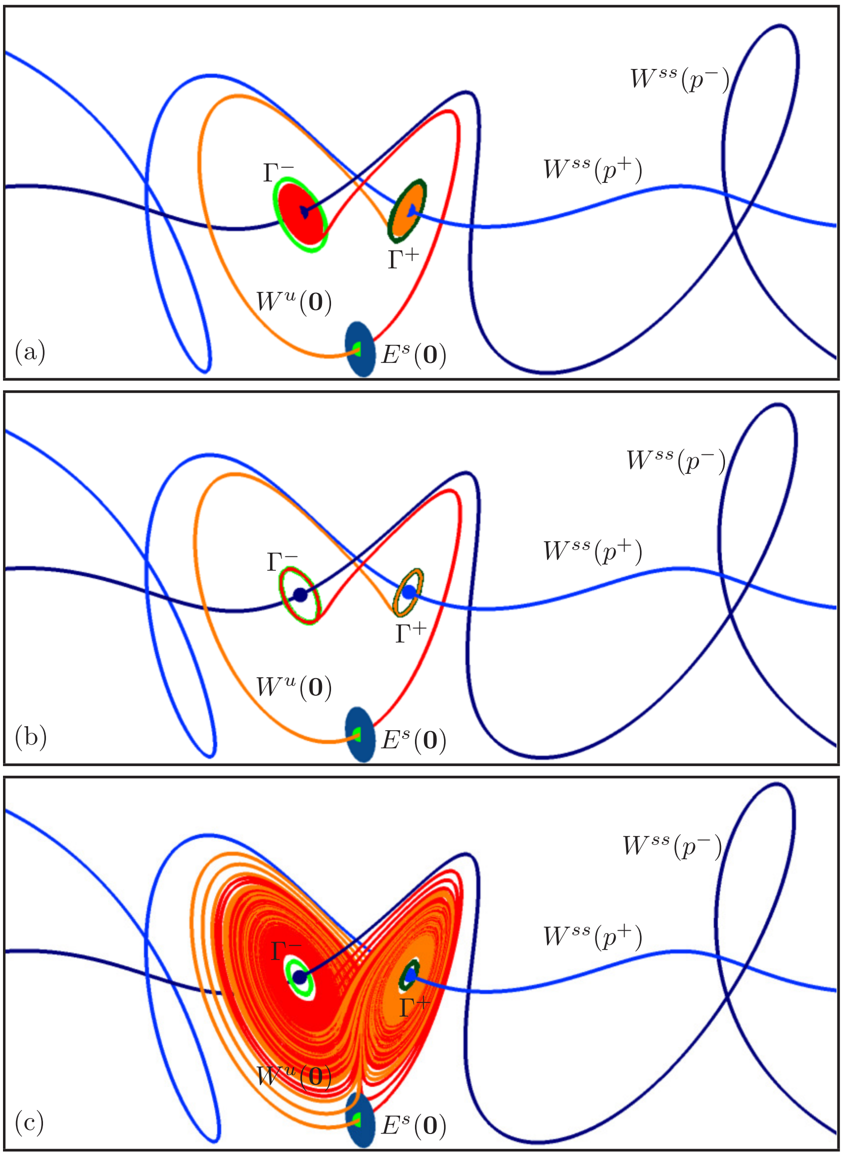

Figure 6: The transition through the EtoP heteroclinic connection at $\varrho_{\rm het} \approx 24.0579$. Shown are $\mathbf{0}$, $p^{\pm}$, $\Gamma^{\pm}$, $W^u(\mathbf{0})$, $W^{ss}(p^{\pm})$, and a small disk in the linear eigenspace $E^s(\mathbf{0})$, for $\varrho = 23.5$ (a), for $\varrho = 24.0579$ (b), and for $\varrho = 24.5$ (c).

show $\widehat{W}^s(\Gamma^+)$ in stereographic projection on both sides of the sphere S_R just before and just after the EtoP heteroclinic connection, respectively; the side with $x \leq 0$ is positioned upside-down below the side with $x \geq 0$, so that the two stereographic projections are connected at their respective south poles. Figure 7(a) shows $\widehat{W}^s(\Gamma^+)$ just before the bifurcation, for $\varrho = 24.047$, illustrating that $\widehat{W}^s(\Gamma^+)$ is part of the indecomposable continuum and covers a large area of S_R; compare with figure 5(d) to identify the primary basins of p^+ and p^- and the area of preturbulence in their complement. As shown in figure 7(b) for $\varrho = 24.060$, just after the bifurcation, $\widehat{W}^s(\Gamma^+)$ consists of only two closed curves on S_R. In particular, this means that the primary basin of p^+ is now bounded only by these two closed curves and no longer involves an arc from $\widehat{W}^s(\mathbf{0})$; the equivalent statement is true for the symmetrically related intersection set $\widehat{W}^s(\Gamma^-)$ which consists of only two closed curves on S_R that form the boundary of the primary basin of p^-.

To help understand the transition for $\widehat{W}^s(\Gamma^+)$ through the EtoP bifurcation, consider in figure 5 the location of the point in $\widehat{W}^{ss}(\mathbf{0})$ with $x \geq 0$ relative to the arcs in $\widehat{W}^s(\Gamma^{\pm})$. When comparing with figure 7, notice that the

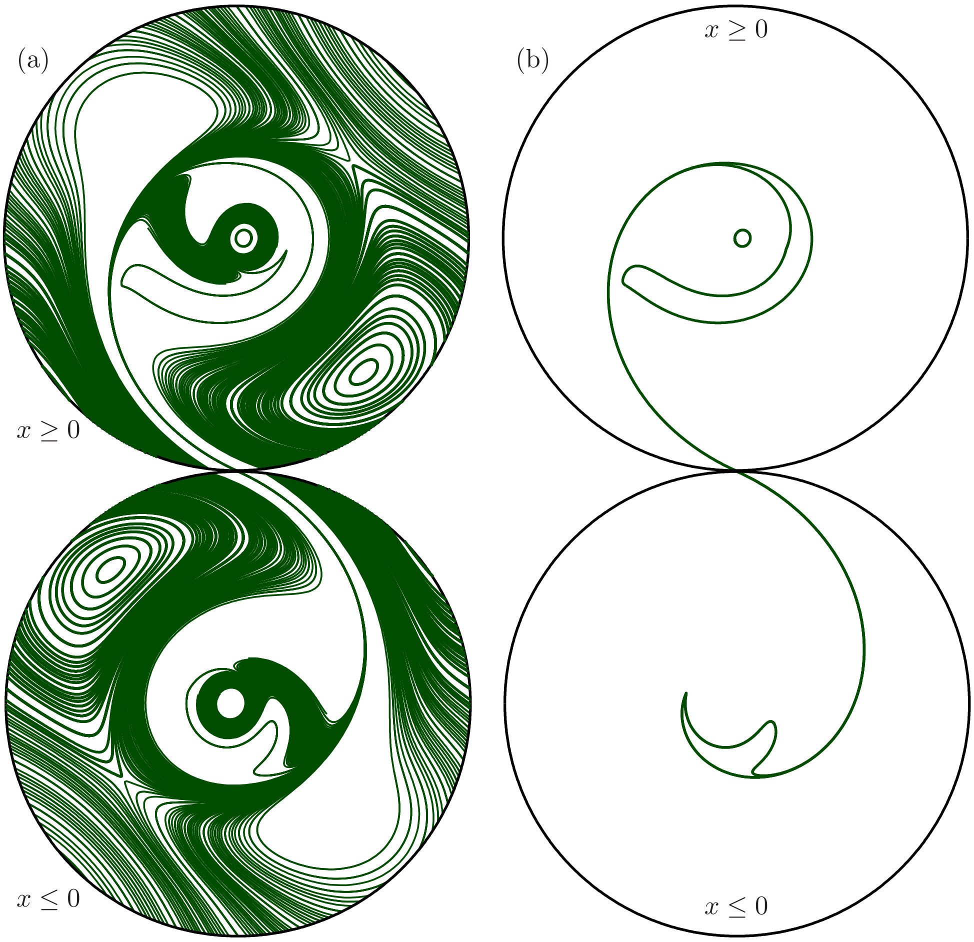

Figure 7: Stereographic projection of $\widehat{W}^s(\Gamma^+)$ on the sphere S_R for $\varrho = 24.047$ with $R = 70.116$ (a) and for $\varrho = 24.060$ with $R = 70.117$ (b).

sharp turn of the central curve at the top of figure 7(a) has effectively 'flipped' to the other side in figure 7(b). The opposite happens for the sharp turn shown in the lower part of panel (b); compare with the symmetric arc in $\widehat{W}^s(\Gamma^-)$ in figure 5(d). In fact, at the EtoP connection, a particular pair of trajectories in $W^s(\Gamma^\pm)$ accumulate on $W^{ss}(\mathbf{0})$ when the two branches of $W^u(\mathbf{0})$ are contained in $W^s(\Gamma^\pm)$.

The EtoP connection gives rise to a chaotic attractor $\mathcal{L}$ formed by the closure of $W^u(\mathbf{0})$; see figure 6(c) for a representative example. Hence, after the EtoP heteroclinic connection, there are three attractors: the two sinks $p^\pm$ and the chaotic attractor $\mathcal{L}$. Since $\widehat{W}^s(\Gamma^+)$ and $\widehat{W}^s(\Gamma^-)$ now bound the basins of p^+ and p^-, respectively, the basin boundary of $\mathcal{L}$ is formed by $W^s(\Gamma^+) \cup W^s(\Gamma^-)$. Hence, the EtoP connection is, in fact, a boundary crisis [18]: as ϱ is decreased toward ϱ_{het} the chaotic attractor increases in size, then hits its own basin boundary $W^s(\Gamma^+) \cup W^s(\Gamma^-)$ and subsequently disappears.

The EtoP connection involves only the unstable manifold $W^u(\mathbf{0})$ and the two stable manifolds $\widehat{W}^s(\Gamma^\pm)$; the Lorenz manifold $W^s(\mathbf{0})$ plays no role in this bifurcation. Figure 8 shows that, indeed, $W^s(\mathbf{0})$ is not affected by the dramatic change in the EtoP connection of $\widehat{W}^s(\Gamma^+) \cup \widehat{W}^s(\Gamma^-)$ — and, hence, of the indecomposable continuum — to two sets of closed curves. The intersection set $\widehat{W}^s(\mathbf{0})$ consists of infinitely many curves before, at and after the EtoP connection. However, the difference after the EtoP connection is that $\widehat{W}^s(\mathbf{0})$ now lies dense in the basin $\widehat{B}(\mathcal{L})$ of the newly created chaotic atractor $\mathcal{L}$; this is illustrated in figure 8(a) for $\varrho = 24.5$, immediately after the EtoP connection. Notice how the set $\widehat{B}(\mathcal{L})$ occupies the complement of the primary basins of p^+ and p^-, which are now their entire basins $\widehat{\mathcal{B}}(p^+)$ and $\widehat{\mathcal{B}}(p^-)$, bounded by $\widehat{W}^s(\Gamma^+)$ and $\widehat{W}^s(\Gamma^-)$,

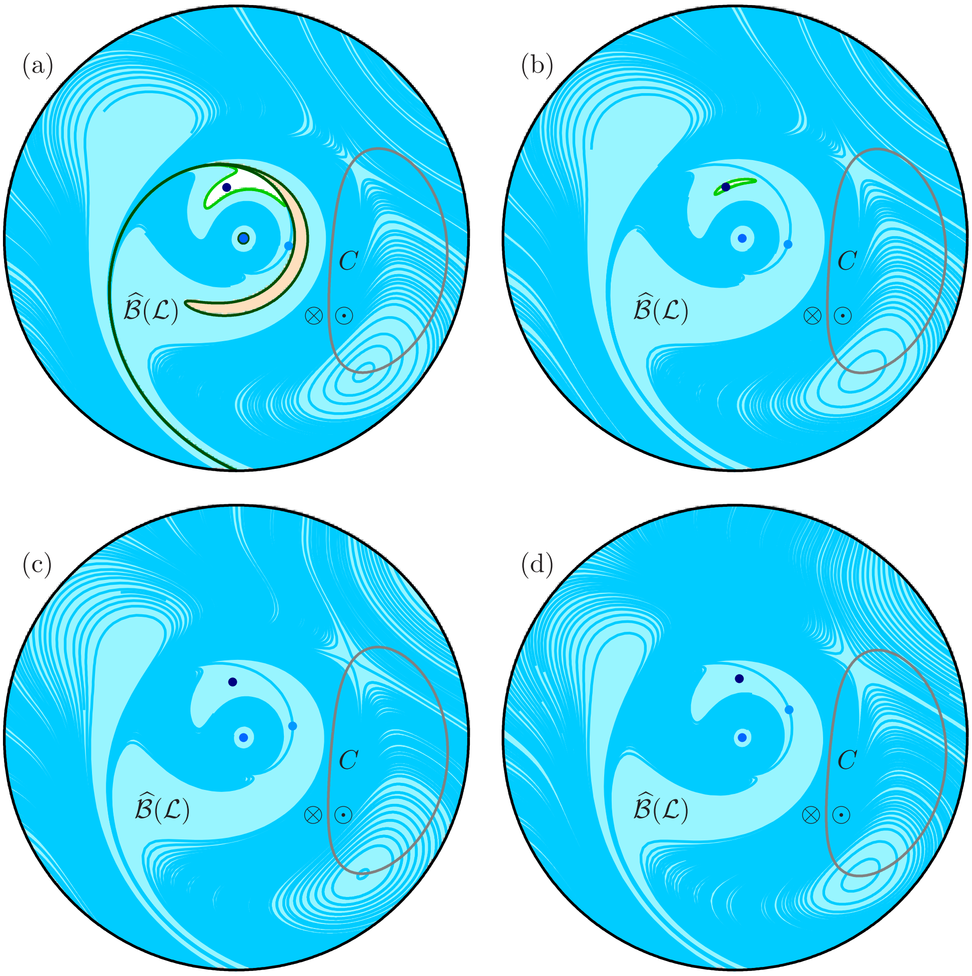

Figure 8: Stereographic projection of S_R for $x \geq 0$, for $\varrho = 24.5$ with $R = 70.186$ (a), for $\varrho = 24.71$ with $R = 70.219$ (b), for $\varrho = 26.5$ with $R = 70.491$ (c), and for $\varrho = 28.0$ with $R = 70.709$ (d), showing how the sets $\widehat{W}^s(\mathbf{0})$ (light blue), $\widehat{W}^s(\Gamma^+)$ (dark green) and $\widehat{W}^s(\Gamma^-)$ (light green) divide S_R into the basins $\widehat{\mathcal{B}}(p^+)$ (sand colour), $\widehat{\mathcal{B}}(p^-)$ (white) and $\mathcal{B}(\mathcal{L})$ (light blue). Also shown are $\widehat{W}^{ss}(0)$ (light blue dot), $\widehat{W}^{ss}(p^+)$ (blue dot) and $\widehat{W}^{ss}(p^-)$ (dark blue dot) and the tangency curve C with the symbols $\otimes$ and $\odot$ indicating the direction of the vector field.

respectively; the closed curve in $\widehat{W}^s(\Gamma^+)$ that surrounds the point $\widehat{W}^{\rm ss}(p^+)$ with $x \geq 0$ can hardly be seen in this figure, because it is only a few pixels wide. As ϱ is increased, the topological circles in $\widehat{W}^s(\Gamma^+)$ and $\widehat{W}^s(\Gamma^-)$ contract to the four points in $\widehat{W}^{ss}(p^\pm)$; see figure 8(b) for $\varrho = 24.71$. The sets $\widehat{W}^s(\Gamma^\pm)$ and $\widehat{\mathcal{B}}(p^-)$ then disappear in the Hopf bifurcation at $\varrho = \varrho_{\rm H} = \frac{470}{19} \approx 24.7368$, where the sinks $p^\pm$ become saddles with one-dimensional stable manifolds, which are continuations of $W^{\rm ss}(p^\pm)$. After the Hopf bifurcation the chaotic attractor $\mathcal{L}$ is the only attractor and $\widehat{W}^s(\mathbf{0})$ is dense in S_R; see figure 8(c) for $\varrho = 26.5$ and figure 8(d) for $\varrho = 28.0$.

Figure 9 illustrates how the larger closed curve in $\widehat{W}^s(\Gamma^+)$, which surrounds the point $\widehat{W}^{ss}(p^+)$ with $x \leq 0$, changes as ϱ is increased. The 'tail' of this closed curve retracts from the side of S_R with $x \geq 0$, a transformation that occurs over a very narrow interval of ϱ-values that is less than 10^{-3} wide. As ϱ is increased further, $\widehat{W}^s(\Gamma^+)$ changes rapidly from the shape it has in figure 7(b) and in figure 8(a) to the more circular shape of (the symmetrically related) $\widehat{W}^s(\Gamma^-)$ in figure 8(b).

Figure 10 illustrates for the classical parameter value $\varrho = 28$ the organization of phase space inside the sphere S_R, whose stereographic projection is shown in figure 8(b). More specifically, S_R is rendered transparent

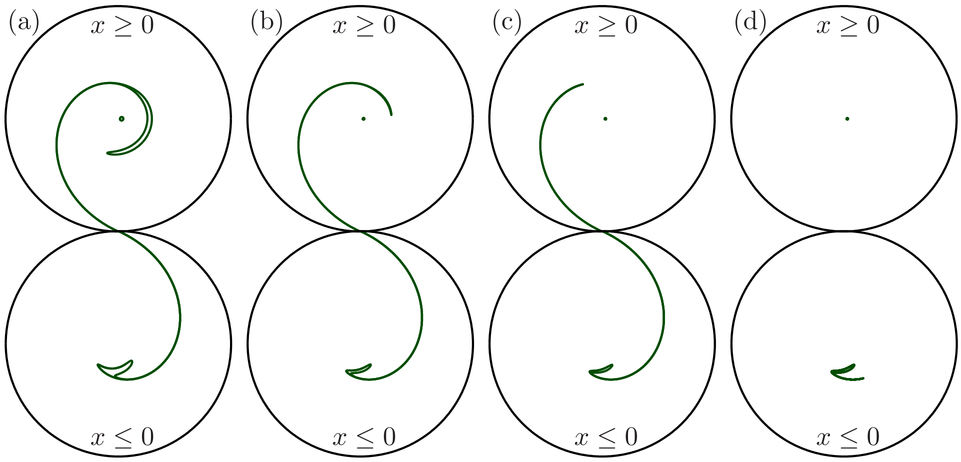

Figure 9: Stereographic projection of $\widehat{W}^s(\Gamma^+)$ on the sphere S_R for $\varrho = 24.6$ with $R = 70.202$ (a), for $\varrho = 24.7$ with $R = 70.217$ (b), for $\varrho = 24.7059473$ with $R = 70.218$ (c), and for $\varrho = 24.7059475$ with $R = 70.218$ (d).

so that we can see the origin $\mathbf{0}$ inside with the two branches of its unstable manifold $W^u(\mathbf{0})$, which accumulate on the Lorenz attractor, and the two saddle points $p^\pm$ with their stable manifolds $W^s(p^\pm)$. Also shown is the part of the Lorenz manifold $W^s(\mathbf{0})$ computed up to geodesic distance 162.5 that lies inside S_R, of which we only render the half with negative y; compare with figure 3(a) and figure 4(a). On S_R we show all computed curves of $\widehat{W}^s(\mathbf{0})$ along with the tangency locus C. Notice in figure 10 how, near p^+, the surface $W^s(\mathbf{0})$ spirals in between trajectories on the Lorenz attractor, and observe that its intersection curves of the shown part with S_R indeed agree with $\widehat{W}^s(\mathbf{0})$. The computed curves of $\widehat{W}^s(\mathbf{0})$ in figure 10 provide a good impression of how the Lorenz manifold fills out the sphere S_R, illustrating how it manages to lie dense in the entire phase space $\mathbb{R}^3$.

5 Computing the intersection sets of invariant manifolds on S_R

The emphasis in this section is on finding the many intersection curves of $W^s(\mathbf{0})$ and $W^s(\Gamma^\pm)$ with S_R by formulating appropriate boundary conditions. The respective 2PBVPs are solved with the package AUTO [12, 13], which implements pseudo-arclength continuation and solves 2PBVPs with orthogonal collocation on piecewise polynomial approximations; see also [6, 9]. This general approach is already discussed in [15, 31]. Here we provide a more detailed explanation that focusses on the issue of computing the respective intersection set when it consists of infinitely many curves, including families of isolas. The Python drivers for these AUTO calculations are available in the form of a demo via the Supplementary Data link.

As a representative example, we consider the computation of $\widehat{W}^s(\mathbf{0}) = W^s(\mathbf{0}) \cap S_R$. Any point in $\widehat{W}^s(\mathbf{0})$ corresponds to a trajectory that starts on S_R and ends at $\mathbf{0}$ as $t \to \infty$. In the computation this trajectory needs to be approximated by an orbit segment with a finite integration time. To this end, the Lorenz system is rescaled by time to yield

$$\dot{\mathbf{u}} = \begin{pmatrix} \dot{u_1} \\ \dot{u_2} \\ \dot{u_3} \end{pmatrix} = T \begin{pmatrix} \sigma(u_2 - u_1) \\ \varrho u_1 - u_2 - u_1 u_3 z \\ u_1 u_2 - \beta u_3 \end{pmatrix}, \tag{3}$$

where the total integration time T is now a parameter. Consequently, any orbit segment satisfying (3) is given over the unit time interval by

$$\mathbf{u} = \{\mathbf{u}(\tau) \in \mathbb{R}^3 \mid 0 \leq \tau \leq 1\}.$$

Hence, any boundary conditions are applied at $\mathbf{u}(0)$ and $\mathbf{u}(1)$, irrespective of the value of T. To compute $\widehat{W}^s(\mathbf{0})$ we define the following two boundary conditions. At $t = 0$, we require

$$\mathbf{u}(0) = \delta \left(\mathbf{v}_1^s \cos(2\pi\,\vartheta) + \mathbf{v}_2^s \sin(2\pi\,\vartheta)\right), \tag{4}$$

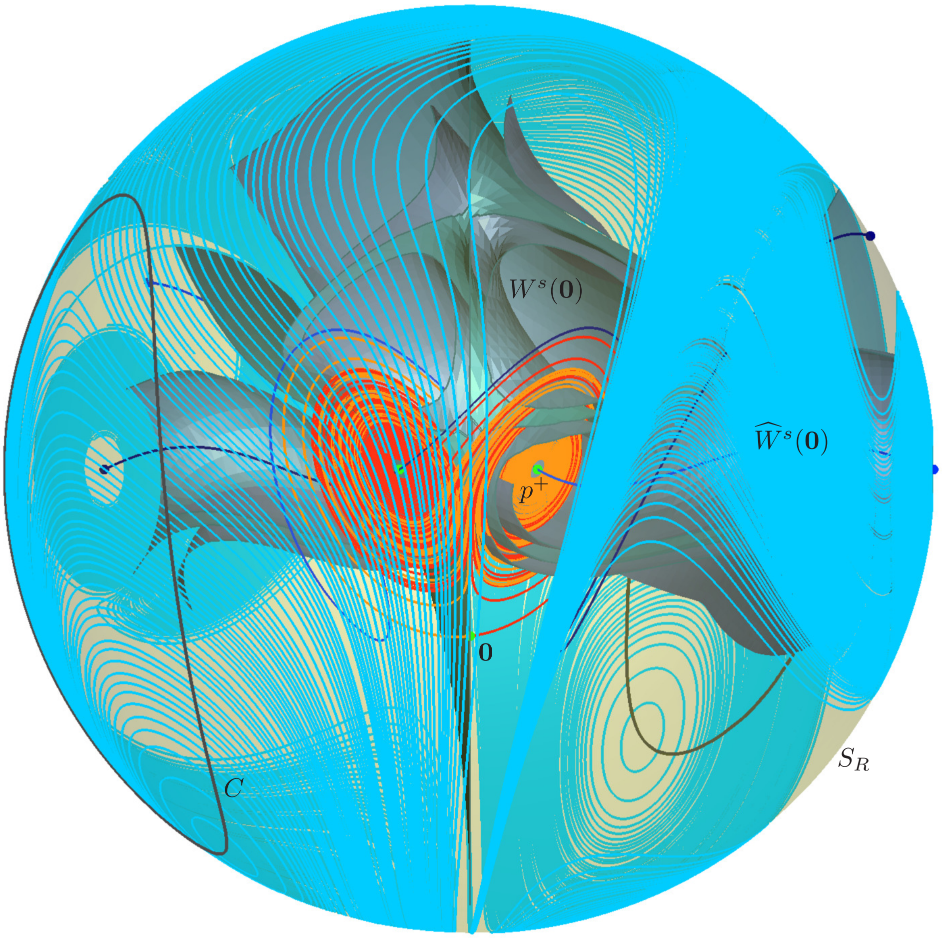

Figure 10: The organization of phase space for $\varrho = 28.0$ inside the sphere S_R with $R = 70.709$. Shown are $\mathbf{0}$, $p^{\pm}$, $W^u(\mathbf{0})$, $W^s(p^{\pm})$, $\widehat{W}^s(\mathbf{0})$, C, and the part of $W^s(\mathbf{0})$, computed up to geodesic distance 162.5, that lies in the region of negative y. See also the accompanying animation dko_tochaos_a03.gif available via the Supplementary Data link.

where $\mathbf{v}_1^s$ and $\mathbf{v}_2^s$ are the two normalized stable eigenvectors at the origin, so that $\mathbf{u}(0)$ lies on a small ellipse (of size δ) in $E^s(\mathbf{0})$ around $\mathbf{0}$; one speaks of a projection boundary condition [7, 8]. At $t = 1$, we require

$$\| \mathbf{u}(1) - (0, 0, \varrho - 1) \|_2 = R, \tag{5}$$

which restricts $\mathbf{u}(1)$ to lie on S_R. For any value of ϑ there is an orbit segment $\mathbf{u}$ with an associated value of T (which is negative in this case) that solves the 2PBVP (3)—(5). Hence, there is an entire one-parameter solution family, which can be computed by continuation in ϑ (with T as a free parameter) once an initial solution segment is known.

Since the z-axis lies in $W^s(\mathbf{0})$, we always know two solutions of the 2PBVP (3)–(4), namely, the two orbit segments that start at $(0, 0, \varrho - 1 + R)$ and $(0, 0, \varrho - 1 - R)$, respectively. Therefore, it is convenient to set $\mathbf{v}_1^s = (0, 0, 1)$ and start the continuation from the known solution for $\vartheta = 0$ given by

$$\mathbf{u}(\tau) = \begin{pmatrix} 0 \\ 0 \\ (\varrho - 1 + R)\, e^{-\beta\,(1-\tau)\,T} \end{pmatrix}$$

with

$$T = \frac{1}{\beta} \ln \left(\frac{\delta}{\varrho - 1 + R} \right).$$

When using the 2PBVP (3)–(4) for $1 < \varrho < \varrho_{\mathrm{hom}}$ we find that the intersection set $\widehat{W}^s(\mathbf{0})$ is traced out by $\mathbf{u}(0)$ as a single closed curve as ϑ varies monotonically from $\vartheta = 0$ to $\vartheta = 1$; for example, see figure 3, where this approach was used to compute $\widehat{W}^s(\mathbf{0})$ for $\varrho = 10$.

5.1 Infinitely many arcs on S_R

As discussed in section 2, as soon as $\varrho_{\mathrm{hom}} < \varrho$, the intersection set $\widehat{W}^s(\mathbf{0})$ consists of infinitely many curves that are arcs whose ends accumulate on either one of two closed curves in $\widehat{W}^s(\Gamma^{\pm})$. Each such arc can be represented as a family of orbit segments solving the 2PBVP (3)–(5), but it would be necessary to find starting orbits on each arc in a systematic way. Moreover, the integration time T goes to (minus) infinity during the computation as each of the limiting closed curves is approached along an arc.

To deal with these issues we perform a computation that selects only those parts of the arcs for which the integration time of the associated orbit segments stays below a preset maximal integration time $T_{\max}$. This is achieved by a single continuation run, where ϑ again varies from 0 to 1 as before, but where boundary condition (5) that requires $\mathbf{u}(0) \in S_R$ is replaced with the boundary condition

$$(T_{\max} - T)\,(R - r) = \varepsilon. \tag{6}$$

Here $r := \| \mathbf{u}(1) - (0, 0, \varrho - 1) \|_2$ is the distance of $\mathbf{u}(1)$ to the centre of the sphere S_R, and $\varepsilon = 10^{-3} \ll 1$ is an accuracy parameter.

The effect of boundary condition (6) is the following. When the continuation of the 2PBVP (3) with (4) and (6) is started from a known solution then we have $r \approx R$ while T is relatively small compared to $T_{\max}$. Hence, boundary condition (6) is satisfied, because $\mathbf{u}(1)$ lies on S_R in very good approximation. During the continuation of a solution family the integration time T increases until $T \approx T_{\max}$. The continuation then proceeds with a solution family that satisfies (6), because $T \approx T_{\max}$, allowing the point $\mathbf{u}(1)$ to retract into the interior of S_R; the associated orbit segments are not part of $\widehat{W}^s(\mathbf{0})$ and the points $\mathbf{u}(1)$ trace out a curve *inside* S_R until an orbit segment is reached for which $\mathbf{u}(0)$ again lies approximately on S_R, that is $r \approx R$. Then the continuation again switches to the continuation of a curve in $\widehat{W}^s(\mathbf{0})$ while $T < T_{\max}$. This process repeats until $\vartheta = 1$; which and how many parts of the arcs in $\widehat{W}^s(\mathbf{0})$ are computed depends on the value of $T_{\max}$. The parts of the single curve traced out by $\mathbf{u}(1)$ that represent curves in $\widehat{W}^s(\mathbf{0})$ are determined in a postprocessing step that selects only those points that lie approximately on S_R; we use the criterion that the corresponding orbit segments have integration time $T \leq \frac{99.9}{100}\, T_{\max}$.

Figure 11 illustrates such a continuation of 2PBVP (3) with (4) and (6) to find arc in $\widehat{W}^s(\mathbf{0})$ with $\varrho = 23$, where we used $R = 69.947$ and $T_{\max} = 8$. Panel (a) shows S_R and the single curve traced out by $\mathbf{u}(1)$; this curve is plotted in light blue when it lies on S_R and dark blue when it lies in the interior of S_R. Panels (b) and (c) show r and T, respectively, plotted against the orbit segment number; there are a total of 644,723 continuation steps taken in this run while ϑ was varied from 0 to 1. Figure 11(b) highlights the orbit segments with $\mathbf{u}(1) \notin \widehat{W}^s(\mathbf{0})$ with $r < R = 69.947$ (dark blue part of the graph) and figure 11(c) highlights the orbit segments with $\mathbf{u}(0) \in \widehat{W}^s(\mathbf{0})$ with $T < T_{\max} = 8$ (light blue part of the graph); compare with panel (a). Notice that the switching between $r \approx R$ and $T \approx T_{\max}$ and vice versa is very rapid due to the fact that $\varepsilon = 10^{-3}$ in (6) is small.

We remark that $\widehat{W}^s(\Gamma^+)$ can also be computed with this approach. Here (4) is replaced by the equivalent boundary condition that $\mathbf{u}(0)$ lies on a vector $\mathbf{v}^s$ in the stable eigenbundle at a small distance from Γ^+ and moves over one (approximate) fundamental domain as the continuation parameter ϑ is varied from 0 to 1. A starting orbit with $\mathbf{u}(1) \in S_R$ is found by continuation in T for fixed $\vartheta = 0$. Since Γ^+ is orientable (has positive Floquet multipliers), the intersection sets of both sides of $W^s(\Gamma^+)$ with S_R need to be computed; for $\varrho_{\mathrm{hom}} < \varrho < \varrho_{\mathrm{het}}$ one side of $W^s(\Gamma^+)$ leads to the infinitely many arcs in $\widehat{W}^s(\Gamma^+)$, while the other side intersects S_R in a single closed curve. We remark that $\widehat{W}^s(\Gamma^-)$ need not be computed separately, because it is the symmetric image of $\widehat{W}^s(\Gamma^+)$.

5.2 Infinitely many isolas on S_R

The emergence of isolas is due to the interaction of the intersection curves in $\widehat{W}^s(\mathbf{0})$ and $\widehat{W}^s(\Gamma^{\pm})$ with the tangency locus C on the sphere S_R. The first curve to form isolas is the curve in $\widehat{W}^s(\Gamma^-)$ that bounds the large

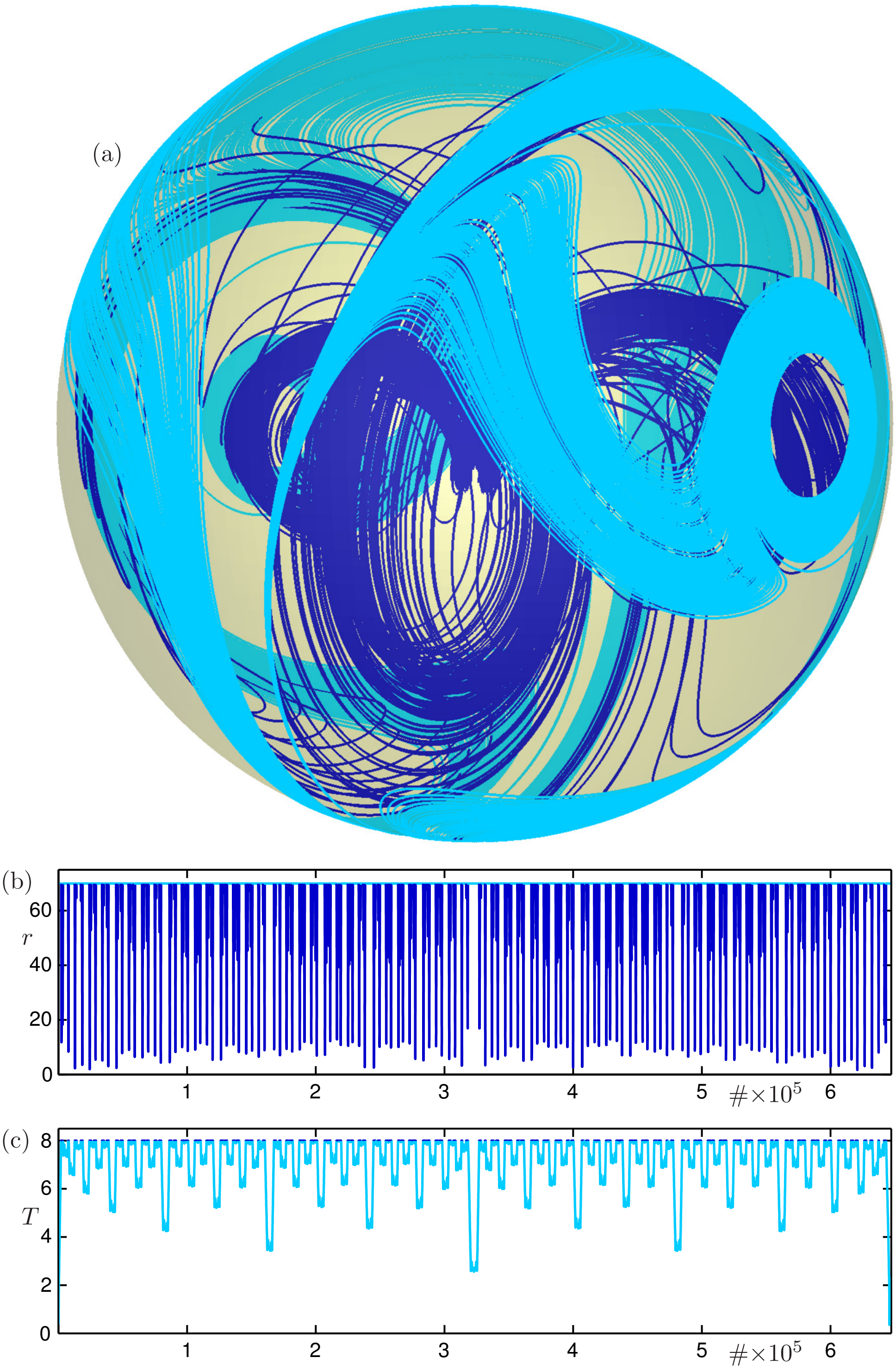

Figure 11: Data from the single continuation run to compute $\widehat{W}^s(\mathbf{0})$ for $\varrho = 23.0$ with $S_R = 69.947$ and $T_{\max} = 8$. Panel (a) shows the curve on S_R traced out by $\mathbf{u}(1)$ of all 644,723 computed orbit segments; there are 275 curve segments of $\widehat{W}^s(\mathbf{0})$ on S_R (light blue) and 274 curve segment inside S_R (dark blue). Panels (b) and (c) show r and T, respectively, as a function of the orbit segment number. See also the accompanying animation dko_tochaos_a04.gif available via the Supplementary Data link.

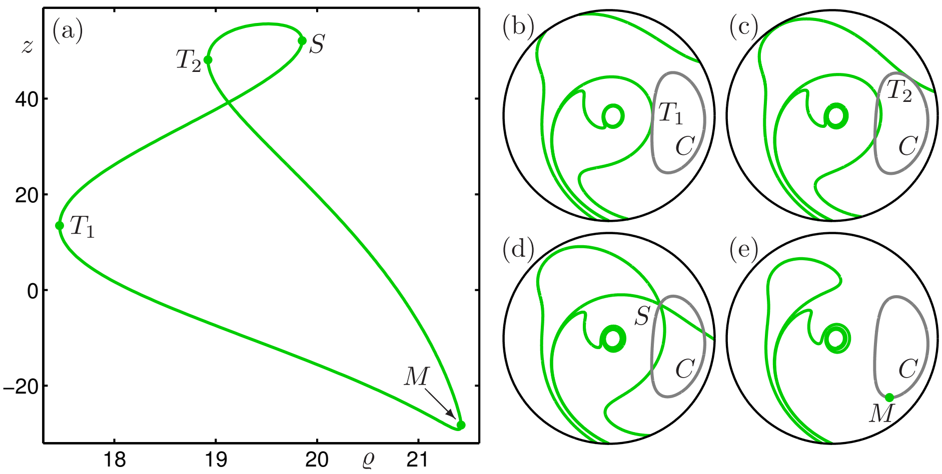

Figure 12: The boundary curve of $\widehat{W}^s(\Gamma^-)$ that forms the first isola on S_R. Panel (a) shows the respective first curve in $\widehat{W}^s(\Gamma^-) \cap C$ in the (ϱ, z)-plane. Panels (b)–(e) are stereographic projections of S_R for $x \geq 0$ that show the corresponding set in $\widehat{W}^s(\Gamma^-)$ at the detected moments of its transitions T_1 at $\varrho = 17.4601$, T_2 at $\varrho = 18.9236$, S at $\varrho = 19.8530$, and M at $\varrho = 21.4200$.

region of $\widehat{\mathcal{B}}(p^-)$ for $\varrho = 19.5$ in figure 5(a). For $\varrho = 21.0$ as in figure 5(b), $\widehat{\mathcal{B}}(p^-)$ has two large regions, one of which is bounded by an isola in $\widehat{W}^s(\Gamma^-)$ — the light green closed curve. Notice that this isola is accumulated by infinitely many other isolas in the sets $\widehat{W}^s(\mathbf{0})$ and $\widehat{W}^s(\Gamma^\pm)$.

The key observation that allows us to compute the isolas in a convenient and systematic way is that they are created by saddle transitions on the tangency locus C, where two local branches join and reconnect differently [32]. In particular, before the saddle transition the respective curve intersects C in four points, and after the saddle transition, the isola intersects C in two points while the other part does not intersect C at all. Finally, as ϱ is increased further, the isola contracts to a single point on C, where it disappears in a minimax transition; indeed the first isola in $\widehat{W}^s(\Gamma^-)$ and the region of $\widehat{\mathcal{B}}(p^-)$ that it bounds have disappeared for $\varrho = 23.0$ as in figure 5(c). The conclusion of this discussion is that the saddle transition and the minimax transition can be detected as fold points (local maxima in ϱ) when one continues in ϱ the intersection points of curves in $\widehat{W}^s(\mathbf{0})$ or $\widehat{W}^s(\Gamma^\pm)$ with C. Such intersection points are defined by the additional boundary condition

$$f(\mathbf{u}(1)) \cdot (\mathbf{u}(1) - (0, 0, \varrho - 1)) = 0; \tag{7}$$

here, $\mathbf{u}(1) \in S_R$ and $\mathbf{u}(1) - (0, 0, \varrho - 1)$ is the normal direction to S_R at $\mathbf{u}$, which implies that the flow is tangent to S_R at $\mathbf{u}(1)$ as soon as (7) holds. Points satisfying this boundary condition can be found by monitoring the left-hand side of (7) during a computation of the respective set of curves for fixed ϱ. Any orbit segment satisfying (7) thus detected can be followed in ϱ, where ϑ and T are also free parameters. Since the tangency locus depends on the radius R of S_R, we allowed R to vary subject to the algebraic condition

$$\begin{aligned} \varrho = a_0 + a_1 R + a_2 R^2 \quad \text{with} \\ a_0 = 2204.380212505092,\ a_1 = -68.520074141368,\ a_2 = 0.533745104664. \end{aligned} \tag{8}$$

This quadratic polynomial was determined by fitting data for the radius R as defined over the ϱ-range considered here.

Figure 12 shows the result of this calculation for the boundary curve of $\widehat{W}^s(\Gamma^-)$ that forms the first isola on S_R. For example, consider the primary basin of p^- for $\varrho = 19.5$ in figure 5(a) and its four intersection points with C. These four points in $\widehat{W}^s(\Gamma^-) \cap C$ lie on a single closed curve in the (ϱ, z)-plane with four fold points with respect to ϱ — two local minima T_1 and T_2 and two local maxima S and M. As panels (b) and (c) show, at T_1 and T_2 the curve in $\widehat{W}^s(\Gamma^-)$ has quadratic tangencies with the curve C, so that immediately past T_2 there are four intersection points C; compare with figure 5(a). The saddle transition at S is illustrated in figure 12(d); notice how the curve connects on C to give rise to an isola; compare with figure 5(b). Hence,

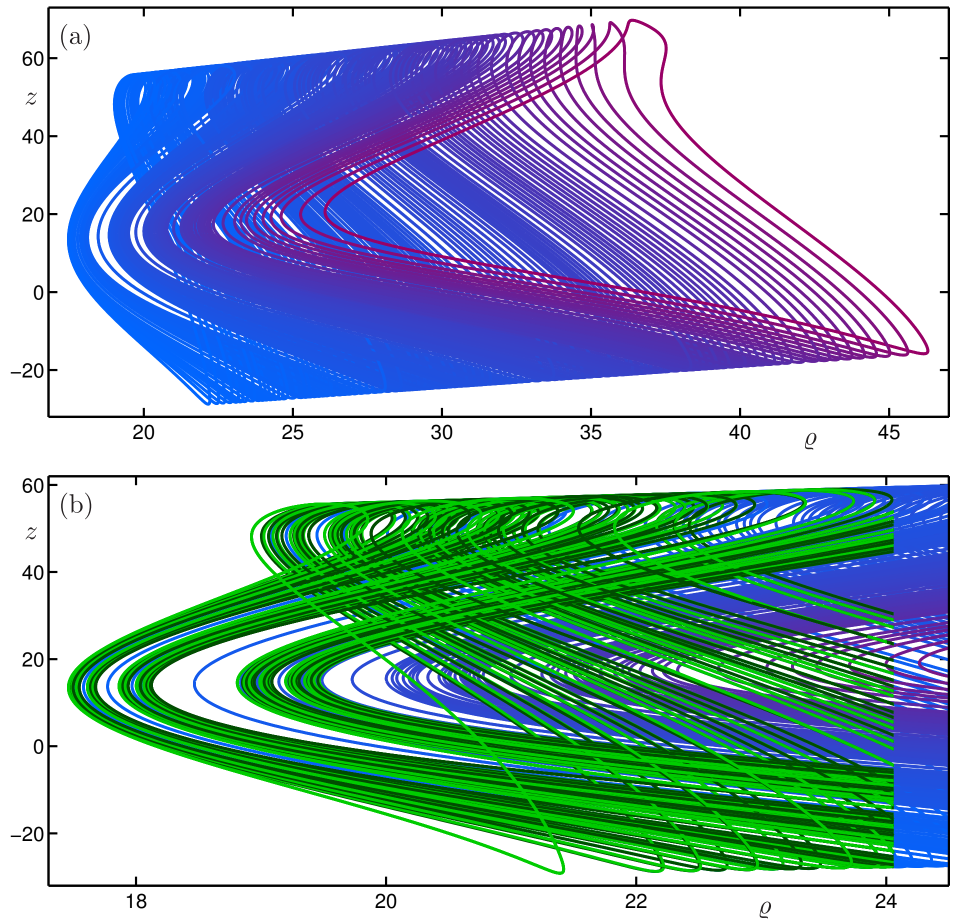

Figure 13: Starting data for the computation of isolas in $\widehat{W}^s(\mathbf{0})$ and $\widehat{W}^s(\Gamma^\pm)$. Panel (a) shows computed curves in $\widehat{W}^s(\mathbf{0}) \cap C$ in the (ϱ, z)-plane, and panel (b) also shows computed curves in $\widehat{W}^s(\Gamma^\pm) \cap C$, which exist only up to the EtoP heteroclinic connection at $\varrho_{\rm het} \approx 24.0579$.

the isola of this first curve in $\widehat{W}^s(\Gamma^-)$ exists for $19.8530 < \varrho < 21.4200$, until it disappears in the minimax transition M illustrated in figure 12(e). Notice, in particular, that the two branches that approach the point M in figure 12(a) correspond to points on the isola; hence, the computation of the isola for any fixed value of ϱ where it exists can be started from this data.

Figure 13 shows all curves in $\widehat{W}^s(\mathbf{0}) \cap C$ and in $\widehat{W}^s(\Gamma^\pm) \cap C$ that can be computed with $T_{\max} = 8$. Panel (a) shows the curves in $\widehat{W}^s(\mathbf{0}) \cap C$ over a large range of ϱ. Panel (b) shows the same curves and also the curves in $\widehat{W}^s(\Gamma^\pm) \cap C$ over a smaller range of ϱ. The curves in $\widehat{W}^s(\Gamma^\pm) \cap C$ do not extend beyond the EtoP heteroclinic connection at $\varrho_{\rm het} \approx 24.0579$, since for $\varrho_{\rm het} < \varrho$ the set $\widehat{W}^s(\Gamma^\pm)$ no longer intersects the tangency locus C; see figure 7(b). Notice that the computed curves in the (ϱ, z)-plane exhibit the same Cantor structure as the associated indecomposable continuum.

The isolas for a fixed value of ϱ can now be computed from the data represented by figure 13; this technique was used to obtain figures 5(b)–(d), 7(a), 8 and 10. Figure 14 illustrates the geometry in phase space behind a single isola in $\widehat{W}^s(\mathbf{0})$ (dark blue closed curve) on S_R for $\varrho = 28$. A part of $W^s(\mathbf{0})$ inside S_R is rendered as a surface; also shown are all the computed curves in $\widehat{W}^s(\mathbf{0})$ that are not isolas. Only one isola is shown, which arises from the thin strip of $W^s(\mathbf{0})$, formed by orbit segments that connect from near the origin to the isola; it is bounded by the two cyan orbits that end exactly on the curve C. When followed from near the origin, where the strip has almost no width, it lies on the initial part of $W^s(\mathbf{0})$ as it folds clockwise around to the back side of the image; the strip then leaves the computed part $W^s(\mathbf{0})$ as it comes back to the front and folds counter-clockwise around the left 'arm' of $W^s(\mathbf{0})$, after which it leaves S_R (somewhere on the other side of sphere) and comes

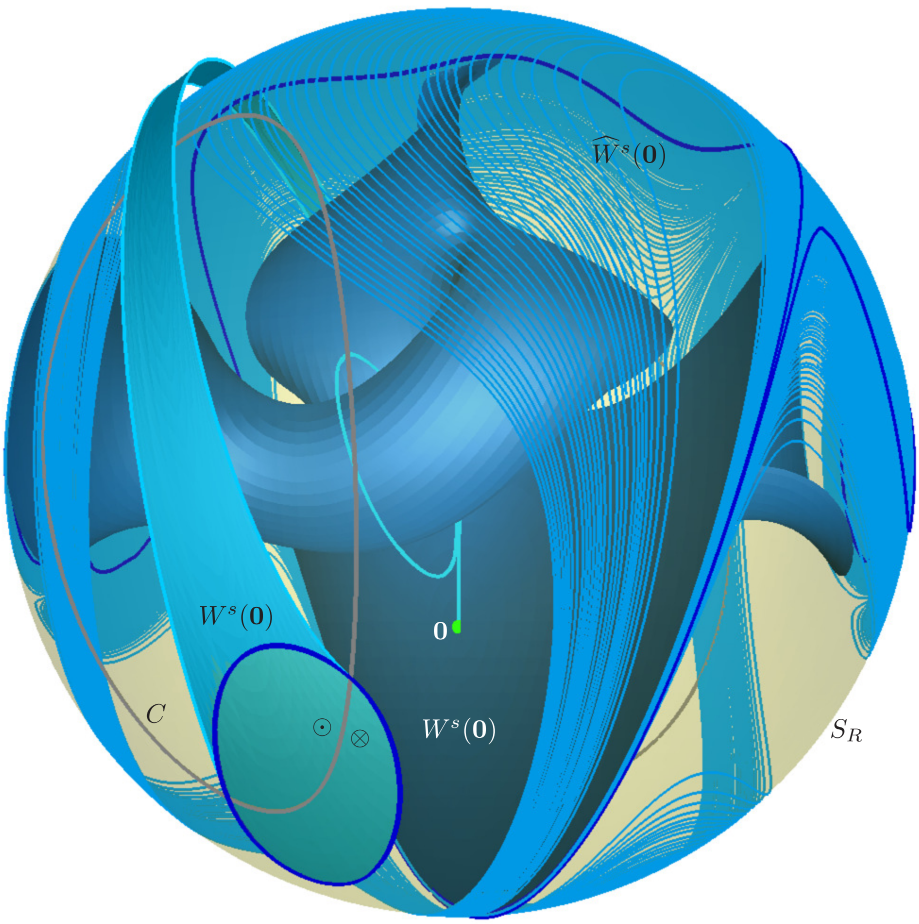

Figure 14: The part of $W^s(\mathbf{0})$ that is used to compute an isola in $\widehat{W}^s(\mathbf{0})$ (dark blue closed curve) on S_R for $\varrho = 28$ with $R = 70.709$; also shown are the curve C with the symbols $\otimes$ and $\odot$ indicating the direction of the vector field, other curves in $\widehat{W}^s(\mathbf{0})$, and the part of $W^s(\mathbf{0})$ inside S_R of total geodesic distance 100. See also the accompanying animation dko_tochaos_a05.gif available via the Supplementary Data link.

back to the front on the outside of S_R. The isola is formed as the strip dips back to intersect S_R in a scoop-like fashion. Hence, the part of $W^s(\mathbf{0})$ bounded by the isola lies again inside S_R.

6 Overall characterization of transition and conclusions

Our findings regarding the transition from simple to chaotic dynamics in the Lorenz system when the parameter ϱ is increased can be formulated as follows; here the numbers 1–5 corresponds to the open ϱ-intervals in figure 1 and the symbols P, hom, EtoP and H to the respective bifurcations.

Statement 1. (Transition to chaos)

1 *Trivial dynamics.* For $0 < \varrho < 1$ the origin $\mathbf{0}$ is a global attractor.

P *Pitchfork bifurcation.* At $\varrho = 1$ the origin $\mathbf{0}$ undergoes a pitchfork bifurcation that creates the two stable equilibria p^- and p^+, while $\mathbf{0}$ becomes a saddle point with one unstable eigenvalue.

2 *Regular attracting dynamics.* For $1 < \varrho < \varrho_{\mathrm{hom}}$ the phase space is divided into the two basins $\mathcal{B}(p^-)$ and $\mathcal{B}(p^+)$ by the two-dimensional stable manifold $W^s(\mathbf{0})$. On any sufficiently large sphere S_R the intersection set $\widehat{W}^s(\mathbf{0})$ is a simple closed curve and $\widehat{\mathcal{B}}(p^+)$ and $\widehat{\mathcal{B}}(p^-)$ are topological disks, that is, simply connected.

hom *Homoclinic bifurcation.* At $\varrho = \varrho_{\rm hom} \approx 13.9265$ the one-dimensional unstable manifold $W^u(\mathbf{0})$ lies in $W^s(\mathbf{0})$ to form a pair of homoclinic orbits of $\mathbf{0}$.

3 *Preturbulent regime.* For $\varrho_{\rm hom} < \varrho < \varrho_{\rm het}$ the phase space is divided into the two basins $\mathcal{B}(p^-)$ and $\mathcal{B}(p^+)$ by $W^s(\mathbf{0})$ and the stable manifold $W^s(\mathcal{S})$ of a hyperbolic set $\mathcal{S}$. The accessible boundary of $\mathcal{B}(p^+)$ is $W^s(\mathbf{0}) \cup W^s(\Gamma^+)$ and the accessible boundary of $\mathcal{B}(p^-)$ is $W^s(\mathbf{0}) \cup W^s(\Gamma^-)$. On any sufficiently large sphere S_R the intersection set $\widehat{W}^s(\mathcal{S})$ is an indecomposable continuum and the two basins $\widehat{\mathcal{B}}(p^+)$ and $\widehat{\mathcal{B}}(p^-)$ are intermingled; moreover, $\widehat{W}^s(\mathcal{S})$ is the closure of $\widehat{W}^s(\Gamma^+) \cup \widehat{W}^s(\Gamma^-)$. As $\varrho \searrow \varrho_{\rm hom}$, the set $\widehat{W}^s(\mathcal{S})$ converges to $\widehat{W}^s(\mathbf{0})$ in the Hausdorff metric and, as $\varrho \nearrow \varrho_{\rm het}$, the set $\widehat{W}^s(\mathcal{S})$ converges to $\widehat{\mathcal{B}}(\mathcal{L})$ in the Hausdorff metric; in particular, the Hausdorff dimension of $\widehat{W}^s(\Gamma^+) \cup \widehat{W}^s(\Gamma^-)$ and the Hausdorff dimension of $\widehat{W}^s(\mathbf{0})$ increase continuously from 1 for $\varrho = \varrho_{\rm hom}$ to 2 for $\varrho = \varrho_{\rm het}$.

EtoP *Heteroclinic bifurcation.* At $\varrho = \varrho_{\rm het} \approx 24.0579$ the two branches of the one-dimensional unstable manifold $W^u(\mathbf{0})$ lie in $W^s(\Gamma^+)$ and $W^s(\Gamma^-)$, respectively, to form a pair of heteroclinic connections between $\mathbf{0}$ and $\Gamma^\pm$.

4 *Turbulent regime with two attracting equilibria.* For $\varrho_{\rm het} < \varrho < \varrho_{\rm H}$ there are three attractors: the stable equilibria $p^\pm$ and a chaotic attractor $\mathcal{L}$. The basins $\mathcal{B}(p^+)$ and $\mathcal{B}(p^+)$ are bounded by $W^s(\Gamma^+)$ and $W^s(\Gamma^-)$, respectively, which are topological cylinders. The basin $\mathcal{B}(\mathcal{L})$ is bounded by $W^s(\Gamma^+) \cup W^s(\Gamma^-)$, and $W^s(\mathbf{0})$ is dense in $\mathcal{B}(\mathcal{L})$. In particular, the Hausdorff dimension of the intersection sets $\widehat{W}^s(\Gamma^\pm)$ on S_R is 1 and the Hausdorff dimension of $\widehat{W}^s(\mathbf{0})$ is 2.

H *Hopf bifurcation.* At $\varrho = \varrho_{\rm H} \approx 24.7368$ the two periodic orbits $\Gamma^\pm$ disappear in a Hopf bifurcation of the equilibra $p^\pm$, which then become saddle foci with one stable eigenvalue.

5 *Turbulent regime of the Lorenz attractor.* For $\varrho_{\rm H} < \varrho \leq 28$ the chaotic attractor $\mathcal{L}$ is the only attractor. Its basin $\mathcal{B}(\mathcal{L})$ is the complement of $p^\pm \cup W^s(p^\pm)$, and $W^s(\mathbf{0})$ is dense in the phase space $\mathbb{R}^3$. In particular, the closure of $\widehat{W}^s(\mathbf{0})$ is S_R.

This above statement is the result of an extensive investigation with highly accurate numerical methods that present the state-of-the-art in invariant manifold computations. While our results concern the full space, they connect perfectly with what is known for the one-dimensional Lorenz map. For example, the saddle hyperbolic set $\mathcal{S}$ in the preturbulent regime corresponds to a Cantor set [46] of the Lorenz map. The indecomposable continuum $\widehat{W}^s(\mathcal{S})$ on S_R is, in fact, its manifestation throughout phase space. Similarly, stated properties of the Hausdorff dimensions of the sets $\widehat{W}^s(\Gamma^+) \cup \widehat{W}^s(\Gamma^-)$ and $\widehat{W}^s(\mathbf{0})$ correspond to the fact that the Cantor set of the Lorenz map changes in Hausdorff dimension from 0 at the homoclinic bifurcation to 1 at the birth of the Lorenz attractor. Strictly speaking, our mathematical observations are mathematical conjectures. On the other hand, the technique of continuing orbit segments defined via suitable two-point boundary problems comes with estimates of convergence. A proof could, therefore, be achieved in principle by error estimates for these types of computations to establish a specific topological property.

The characterization in Statement 1 of the properties of the global manifolds in the different regions and the bifurcations between them is generic, meaning that the transition to chaos will be qualitatively the same along any suitable path that crosses the homoclinic, EtoP and Hopf bifurcations. Indeed, for example, in the (ϱ, σ)-plane, these bifurcations form curves that delimit regions 1–5 with the respective global organization of the phase space of the Lorenz system. Figure 15 shows the bifurcation diagram with the curves hom, EtoP and H in a suitable part of the (ϱ, σ)-plane. Preturbulence can be found in region 3, and a chaotic attractor in regions 4 and 5.

We remark that the chaotic dynamics in the Lorenz system is no longer described by a one-dimensional map once ϱ is too large, the so-called foliation condition fails and there appear hooked horseshoes in the Poincaré return map [2, 42]. As will be reported elsewhere, the boundary where the foliation condition fails can be continued in all parameters with a boundary value problem setup; for $\sigma = 10$ it lies at $\varrho \approx 31.01$. Moreover, there is a plethora of other phenomena for larger values of ϱ, including windows of attracting periodic orbits and period-doubling to chaos [38, 42] and families of codimension-two T-point bifurcations [10].

The investigation of the specific example of the Lorenz equations showcases, more generally, what can be achieved with advanced methods for the computation of global invariant manifolds. We argue that these

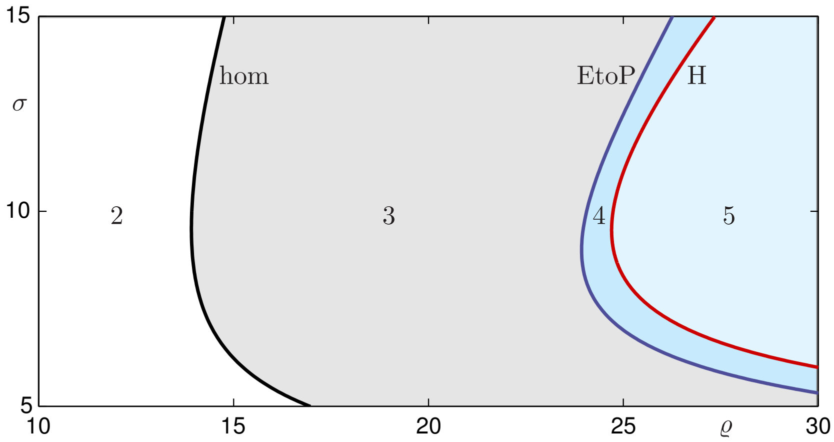

Figure 15: Bifurcation diagram of (1) in the (ϱ, σ)-plane, showing the curves hom of homoclinic bifurcation of $\mathbf{0}$, EtoP of heteroclinic connection from $\mathbf{0}$ to $\Gamma^{\pm}$, and H of Hopf bifurcation; regions 2 to 5 from Statement 1 are labelled and shaded.

methods have reached such a maturity that detailed topological and geometric statements can be made about the overall organization of phase space. The Python drivers for the calculations presented here are available as an AUTO demo file via the Supplementary Data link.

Indeed, other dynamical systems can be studied in the same spirit. Recent examples are the study of global invariant manifolds near a Shilnikov homoclinic bifurcation in [5] and near codimension-two inclination and orbit flip bifurcations [4]. Apart from such more theoretical studies, the computation of global invariant manifolds is also an important tool for understanding concrete phenomena in applications, including basins of attraction in neuronal cells [34], the emergence of mixed-mode bifurcations [11], and excitability of transient spikes [36].

Acknowledgements

We would like to thank John Guckenheimer for helpful discussion on the Lorenz system over many years. We also thank Jennifer Creaser for her careful reading of a draft of this manuscript. The research of EJD was supported by NSERC (Canada) Discovery Grant N00138, and BK and HMO acknowledge the hospitality of Concordia University during our regular visits.

References

References

[1] Abraham R H and Shaw C D 1985 *Dynamics — the geometry of behavior, Part three: global behavior* (Santa Cruz: Aerial Press).

[2] Afrajmovich V S, Bykov V V and Sil'nikov L P 1977 The origin and structure of the Lorenz attractor. (Russian) *Dokl. Akad. Nauk SSSR* **234**(2) 336–339.

[3] Aguirre P, Doedel E J, Krauskopf B and Osinga H M 2011 Investigating the consequences of global bifurcations for two-dimensional invariant manifolds of vector fields *Discr. Contin. Dynam. Syst. – Ser. A* **29**(4) 1309–1344

[4] Aguirre P, Krauskopf B and Osinga H M (2013) Global invariant manifolds near homoclinic orbits to a real saddle: (non)orientability and flip bifurcation, *SIAM J. Appl. Dyn. Syst.* **12**(4) 1803–1846

[5] Aguirre P, Krauskopf B and Osinga H M (2014) Global invariant manifolds near a Shilnikov homoclinic bifurcation, *J. Comput. Dyn.* **1**(1) 1–38

[6] Ascher U M, Christiansen J and Russell R D 1981 Collocation software for boundary value ODEs, *ACM Trans. Math. Software* **7**(2) 209–222

[7] Beyn W-J 1990 The numerical computation of connecting orbits in dynamical systems *IMA J. Numer. Anal.* **10**(3) 379–405

[8] Beyn W-J 1990 Global bifurcations and their numerical computation *Continuation and Bifurcations: Numerical Techniques and Applications* Proc. NATO Advanced Research Workshop (Leuven, Belgium) Nato Science Series C Vol. 313 ed D Roose, B de Dier and A Spence (Dordrecht: Kluwer) pp. 169–181

[9] Boor C de and Swartz B 1973 Collocation at Gaussian points, *SIAM J. Numer. Anal.* **10**(4) 582–606

[10] Creaser J L, Krauskopf B and Osinga H M (in press) α-flips and T-points in the Lorenz system *Nonlinearity*

[11] Desroches M, Guckenheimer J, Krauskopf B, Kuehn C, Osinga H M and Wechselberger M (2012) Mixed-mode oscillations with multiple time scales *SIAM Review* **54**(2) 211-288

[12] Doedel E J 1981 Auto, a program for the automatic bifurcation analysis of autonomous systems *Congr. Numer.* **30** 265–384

[13] Doedel E J 2007 Auto-07P: Continuation and bifurcation software for ordinary differential equations, with major contributions from Champneys A R, Fairgrieve T F, Kuznetsov Yu A, Oldeman B E, Paffenroth R C, Sandstede B, Wang X J and Zhang C; available at `http://cmvl.cs.concordia.ca/auto/`

[14] Doedel E J, Krauskopf B and Osinga H M 2006 Global bifurcations of the Lorenz manifold *Nonlinearity* **19**(12) 2947–2972

[15] Doedel E J, Krauskopf B and Osinga H M (2011) Global invariant manifolds in the transition to preturbulence in the Lorenz system, *Indag. Math. (N.S.)* **22**(3–4) 222–240

[16] Gleick J 1988 *Chaos: Making a New Science* (London: Heinemann)

[17] Glendinning P and Sparrow C 1984 Local and global behavior near homoclinic orbits *J. Statist. Phys.* **35**(5/6) 645–696.

[18] Grebogi C, Ott E and Yorke J A 1984 Crises, sudden changes in chaotic attractors, and transient chaos *Physica D* **7** 181–200

[19] J Guckenheimer. A strange, strange attractor. In J E Marsden and M McCracken (Eds.) *The Hopf bifurcation and its applications*, pp. 368–381. Springer, 1976.

[20] Guckenheimer J and Holmes P 1986 *Nonlinear Oscillations Dynamical Systems and Bifurcations of Vector Fields*, Second Printing (New York: Springer-Verlag).

[21] Guckenheimer J and Williams R 1979 Structural stability of Lorenz attractors *Publ. Math. IHES* **50** 59–72

[22] Jackson E A 1985 The Lorenz system: I. The global structure of its stable manifolds *Phys. Scr.* **32**(5) 469-475

[23] Jackson E A 1985 The Lorenz system: II. The homoclinic convolution of the stable manifolds *Phys. Scr.* **32**(5) 476-481

[24] Kaplan J L and Yorke J A 1979 Preturbulence, a regime observed in a fluid flow model of Lorenz *Comm. Math. Phys.* **67** 93–108

[25] Kennedy J A (1993) How indecomposable continua arise in dynamical systems; in *Papers on General Topology and Applications*, Seventh Summer Conference at the University of Wisconsin *Annals of the New York Academy of Science* **704** 180–201

[26] Kennedy J A (1995) A brief history of indecomposable continua *Modern Methods in Continuum Theory* (*Lecture Notes in Pure Appl. Math. vol 179*) ed H Cook, W Ingram, K Kuperberg, A Lelek and P Minc (New York: Marcel Dekker) pp. 103–126

[27] Kennedy J A and Yorke J A (1995) Bizarre topology is natural in dynamical systems *Bull. Amer. Math. Soc. (N.S.)* **32** 309–316

[28] Krauskopf B and Osinga H M 1999 Two-dimensional global manifolds of vector fields *Chaos* **9**(3) 768–774

[29] Krauskopf B and Osinga H M 2003 Computing geodesic level sets on global (un)stable manifolds of vector fields *SIAM J. Appl. Dyn. Sys.* **4**(2) 546–569

[30] Krauskopf B and Osinga H M 2007 Computing invariant manifolds via the continuation of orbit segments; *Numerical Continuation Methods for Dynamical Systems* Underst. Complex Syst. ed B Krauskopf, H M Osinga and J Galán-Vioque (New York: Springer-Verlag) pp 117–154

[31] Krauskopf B, Osinga H M, Doedel E J, Henderson M E, Guckenheimer J, Vladimirsky A, Dellnitz M and Junge O 2005 A survey of methods for computing (un)stable manifolds of vector fields *Int. J. Bifurcation and Chaos* **15**(3) 763–791

[32] Lee C M, Collins P J, Krauskopf B and Osinga H M (2008) Tangency bifurcations of global Poincaré maps *SIAM J. Appl. Dynam. Syst.* **7**(3) 712–754

[33] Lorenz E N 1963 Deterministic nonperiodic flows *J. Atmospheric Sci.* **20** 130–141

[34] Nowacki J, Mazlan S H, Osinga H M and Tsaneva-Atanasova K T (2010) The role of large-conductance calcium-activated K^+ (BK) channels in shaping bursting oscillations of a somatotroph cell model *Physica D* **239**(9) 485-493

[35] Osinga H M and Krauskopf B 2002 Visualizing the structure of chaos in the Lorenz system *Computers and Graphics* **26**(5) 815–823

[36] Osinga H M and Tsaneva-Atanasova K T (2013) Geometric analysis of transient bursts *Chaos* **23**(4) 046107

[37] Perelló C 1979 Intertwining invariant manifolds and Lorenz attractor; in *Global theory of dynamical systems (Proc. Internat. Conf., Northwestern Univ., Evanston, Ill., 1979)*, Lecture Notes in Math. **819**, (Berlin: Springer-Verlag) pp. 375–378.

[38] Robbins K 1979 Periodic solutions and bifurcation structure at high r in the Lorenz model at $\sigma = 10$ *SIAM J. Appl. Math.* **36** 457–472.

[39] Ruelle D and Takens F (1971) On the nature of turbulence, *Commun. in Math. Phys.* **20**(3) 167–192

[40] Sanjuán M A F, Kennedy J A, Ott E and Yorke J A (1997) Indecomposable continua and the characterization of strange sets in nonlinear dynamics, *Phys. Rev. Lett.* **78**(10) 1892–1895

[41] Simó C (2003) personal communication at *Equadiff 2003*, Hasselt, Belgium.

[42] Sparrow C 1982 *The Lorenz Equations: Bifurcations, Chaos and Strange Attractors* (*Applied Mathematical Science vol 41*) (New York: Springer-Verlag).

[43] Tucker W 1999 The Lorenz attractor exists *Comptes Rendus de l'Académie des Scienes Série I. Mathématique* **328**(12) 1197–1202.

[44] Viana M 2000 What's new on Lorenz strange attractors? *Math. Intelligencer* **22**(3) 6–19.

[45] Williams R F 1979 The structure of Lorenz attractors *Publ. Math. IHES* **50** 101–152.

[46] Yorke J A and Yorke E D 1979 Metastable chaos: the transition to sustained chaotic behavior in the Lorenz model *J. Stat. Phys.* **21**(3) 263-277